Wave equation inversion for simultaneous reconstruction of electric conductivity and dielectric permittivity in 2D with a CSEM method at the intermediate frequency range.

*François Bretaudeau**, *Romain Brossier*†, *Bernard Bourgeois**.

ABSTRACT

Determining the electric properties of the first tens of meters is a major issue for many applications in water ressource management, environnement or risk assessment. Electromagnetic methods (EM) are methods of choice as they allow a rapid non contact acquisition of geophysical data and are highly sensitive to the electric properties of soils. However, low frequency diffusive EM methods ($<$30 kHz) provide a limited resolution at very shallow depth and are not sensitive to the dielectric permittivity. On the other hand, Ground Penetrating Radar (GPR) is a high frequency EM propagative method ($>$30 MHz) mainly sensitive to the variations of permittivity that often have a very limited penetration depth. So far the intermediate frequencies range has been very fewly investigated because of acquisition difficulties. However, it is the ideal frequency range to investigate quantitatively those shallow depth with a satisfying resolution. Furthermore, EM waves at those frequencies are sensitive to both conductivity and permittivity.

Propagation of EM waves at the intermediate frequencies range is such that both propagative and diffusive terms of the Helmoltz equation have to be considered. We investigate here the potential of frequency-domain wave-equation inversion to simultaneously reconstruct the distributions of conductivity and permittivity in 2D. The full EM wave equation is considered including both propagative and diffusive terms, and is solved with a Discontinuous-Galerkin Finite-Element modeling solver. In a manner similar to seismic full waveform inversion, the inversion strategy proposed here relies on a quasi-Newton optimization and an adjoint-state formulation to avoid explicit computation of the sensitivity matrix. We illustrate the potential of this joint inversion on synthetic tests.

INTRODUCTION

Imaging the electrical properties of the 10th to 30th meters is nowaday a major issue for many applications in land planning, natural and anthropic risk assessment, and water ressources management. Direct current eletric method (DC) and low frequency eletromagnetic methods (EM) are both commonly used to provide information in 1D, 2D and even now in 3D of the eletric conductivity. The now very popular DC method (Dahlin, 2001; Loke and Barker, 1996) is limited in productivity because it requires to place electrodes. On the other hand, in purely magnetic mode (sources and receivers are coils), controlled source eletromagnetic method (CSEM) is well adapted to fast and long profiling because it does not require any contact. In other modes, it is also possible to use fixed receiver stations and to move the source, as for instance in marine CSEM (Constable and Srnka, 2007). However, processing tools for CSEM data conventionaly acquired on near surface and environnemental geophysics assumes that EM waves are in a low frequency diffusive regime. As a consequence the usable frequencies (f<30 kHz) does not allow to access to the conductivity of the first few meters with a high resolution. On the contrary, ground penetrating radar (GPR) assumes mainly propagative waves by working at high frequency (f>30 MHz). Although several authors also tried to reconstruct the conductivity at those frequencies (Holliger et al., 2001; Lavoué et al., 2014), GPR is in general mainly sensitive to spatial variations of permittivity, especially when ground based acquisition is used, and is limited to moderate investigation depth (<3 m in the presence of conductive layers such as clays). None of the existing EM methods are adapted for sounding the 3 first thenth meters with a high resolution, and joint reconstruction of both permittivity and conductivity is in general not possible. However, with the improvement of EM acquisition system that allow reliable recording of higher frequencies (up to a few hundreds kHz), in particular in airborne EM, a few authors started to highlight that accurate mapping of the conductivity requires to acount for the dielectric permittivity in the modeling, and even investigate on the possibility of mapping the surface permittivity (Huang and Fraser, 2001, 2002)

A few authors (Stewart et al., 1994; Tabbagh, 1994; Bourgeois, 2002; Wallin, 2010; Kessouri et al., 2012) started to assess the potential of a frequency domain EM sounding in the frequency range intermediate between the low frequency diffusive regime and the high frequency propagative regime. They have shown how EM waves in this intermediate frequency range ($\sim$ 30 kHz to 30 MHz) are sensitive both to conductivity and permittivity, and how this regime can be exploited to sound the shallow subsurface with a high resolution, and to access to quantitative estimations of the dielectric permittivity. Up to now, the inversion process proposed by those authors is limited to homogeneous model (Kessouri et al., 2012) or 1D layered model (Bourgeois, 2002). However, in many cases, the 1D assumption is too restrictive, in particular in the highest range of frequencies. Reconstruction of heterogeneous media would require 2.5D or 3D inversion, and obvisouly an efficient a 2.5 or 3D modeling strategy.

There is a large variety of numerical modeling strategies for simulating EM waves propagation depending of the nature of the data or the simplifications of the model that are done. At the GPR frequencies, the modeling and imaging tools are usually derived from reflection seismic tools and thus rely on ray theory, such as traveltime tomography, velocity analysis and migration (Cai and McMechan, 1995; Holliger et al., 2001; Fisher et al., 1992a,b; Bitri and Grandjean, 1998). Finite-difference or finite-element methods in the time domain (Lampe et al., 2003), but also in the frequency domain (Lopes, 2009; Lavoué et al., 2014) are becoming more and more common with increasing performances of computing capabilities and emergence of Full Waveform Inversion of cross-hole and ground-based GPR data (Ernst et al., 2007; Lopes, 2009; Meles et al., 2010, 2011; Cordua et al., 2012; Lavoué et al., 2014). At deep CSEM and MT frequencies as well as for shallow CSEM and airborne EM, authors often used very efficient semi-analytical formulations (Chave and Cox, 1982; Loseth and Ursin, 2007; Streich et al., 2011) or integral equation methods (Wannamaker et al., 1984; Avdeev et al., 2002). An overview is given in Avdeev (2005). In general, the dielectric permittivity is not considered because it has negligible influence at low frequencies. Finte-difference (Newman and Alumbaugh, 1995; Weiss and Newman, 2002; Streich, 2009; Streich et al., 2011) or finite-element methods (Badea et al., 2001; Mitsuhata and Ushida, 2004) are common in the frequency domain, and efficient methods are emerging also in the time domain (Wang and Hohmann, 1993; Oldenburg et al., 2007; Borner et al., 2008). Integral-equation methods are very efficient and accurate for models with simple geometries, however their complexity increases with the complexity of the model. In contrast, the computational cost of FD or FE methods is less dependant on the degree of heterogeneities of the investigated domain, making those approaches more adapted to 2D or 3D inversion of complex natural media. Here again, the dielectric permittivity is generally not considered, or when it is, it has no influence at the frequency of interest. Most numerical modeling techniques result in a linear system of equation $\mathbf{Au} = \mathbf{s}$, where the matrix $\mathbf{A}$ is the propagation operator, $\mathbf{u}$ represents the vector of unkonwn, and $\mathbf{s}$ the source terms. To solve this kind of system, iterative or direct solver are available, each approach being more adapted depending on how is built the matrix $\mathbf{A}$, the number of right-hand-side terms in $\mathbf{s}$, and the computing limitations imposed by the computing machine (memory, number of core available) or the operator (computational time). For instance, Streich (2009), Streich et al. (2011) and Abubakar et al. (2008) proposed to use a direct solver to solve the 2.5 and 3D CSEM problems with frequency-domain finite-difference. They all argue in favor of direct solvers because of their robustness compared to iterative solvers in presence for instance of strong conductivity variations, and because multisource solutions can be obtained for little additional cost. In their formulation, the permittivity is introduced in the matrix $\mathbf{A}$ as it is straightforward and does not cost more, but it has no influence at all at the marine CSEM frequencies they are interested in. Such a modeling scheme should be also used at higher frequencies, however, the conditionning of the matrix and the boundary conditions would be less adapted, especially when propagative effects become significant.

In this paper, we propose to investigate a general framework to perform inversion in heterogeneous media that would be valid when no simplification of the Helmoltz equation according to its propagative or diffusive regime or its heterogeneity can be done. In this configuration, the inversion of EM data is in fact similar to a frequency domain wave equation tomography, as it now becomes common is seismic exploration. Our approach is thus largely inspired by the Full Seismic Waveform Inversion (FWI) (Tarantola, 1984; Virieux and Operto, 2009) proposed in the frequency domain by Pratt and Worthington (1990). However, in this case we do not invert only the seismic wave speed, but both the permittivity and conductivity that are related to real and imaginary parts of the complex wavenumber. The approach is also quite similar to what was recently proposed by Plessix and Mulder (2008) and by Grayver et al. (2013) for 3D inversion of marine CSEM data, or by Avdeev and Avdeeva (2009) for 3D magnetotelluric data inversion, however, the regime they used is purely diffusive and only the conductivity is inverted.

Usually, in wave-equation inversion, the forward problem is solved with a FD or FE method, and for practical reasons, although it is not essential, the inversion grid is generaly the same or a subset of the modeling grid, leading to a pixel-like inversion. Due to the large number of parameters to be inverted, the Fréchet kernels are in general too expensive to be computed explicitely. Thus the gradient of the misfit function is computed using an adjoint-state method (Plessix, 2006). The inversion is then solved using a gradient-based descent method. The trade-off between the various classes of parameters can be treated by using an approximation of the Hessian with a quasi-newton l-BFGS optimization algorithm and a preconditionner.

In the first part of the paper we describe the methodology. We detail the modeling of EM waves and validate using a small square example. Then we explain how the gradient of the misfit function is computed, and validate the inversion scheme using a synthetic example. In the second part, we present a more realistic syntetic case with standard surface-surface acquisition geometry. Discussion and conclusions are given in the last part.

METHODOLOGY

Solving the forward problem in EM at intermediate frequencies

In the intermediate frequency range ($\sim$30 kHz - 30 MHz), both diffusive and propagative terms of the Helmoltz equation have a significant contribution. Therefore, contrary to controlled source electromagnetic method (CSEM) at lower frequencies, or at higher frequency with ground penetrating radar (GPR), no simplification can be done. The complete Helmoltz equation have to be considered:

$$\nabla^2 \mathbf{h}(\mathbf{x}, \omega) + k(\mathbf{x}, \omega)^2 \mathbf{h}(\mathbf{x}, \omega) = \mathbf{b}(\mathbf{x}, \omega), \tag{1}$$

where $\mathbf{h}(\mathbf{x}, \omega)$ is the magnetic field, $\mathbf{b}(\mathbf{x}, \omega)$ is the source excitation and $k(\mathbf{x}, \omega)$ the complex wavenumber. $\mathbf{x}$ denotes position in the investigated domain and ω the pulsation. The wavenumber k describes the domain using the spatial distribution of its eletromagnetic properties.

k is a function of the electric conductivity $\sigma(\mathbf{x})$, the dielectric permittivity $\varepsilon(\mathbf{x})$ and the magnetic permeability $\mu(\mathbf{x})$ as a function of space, and of the pulsation ω:

$$k(\sigma, \varepsilon, \mu, \omega)^2 = \mu\varepsilon\omega^2 - i\mu\sigma\omega. \tag{2}$$

For the sake of clarity, the spatial dependency in equation 2 and in the rest of the article is not written explicitely. We also define the electric resistivity $\rho = \frac{1}{\sigma}$, the relative permittivity $\varepsilon_r = \frac{\varepsilon}{\varepsilon_0}$ and the relative magnetic permeability $\mu_r = \frac{\mu}{\mu_0}$. The real part of k controls the displacement currents whereas the conduction currents are governed by the conductivity, that is by the imaginary part of k. From a wave propagation point of vue, the real part of the wavenumber k controls the propagative behavior of the wavefield, whereas the imaginary part controls its attenuation. At the GPR frequencies (>30 MHz), the real part of k which depends on ω^2 is usually much larger than the imaginary part so it has a moderate influence. EM waves at those frequencies are dominated by displacement currents. In particular, the imaginary part has very little influence on the phase of the propagating wave. For this reason it is often neglected and the GPR is considered as a purely propagative method. On the contrary, at low frequency (<30 kHz), the imaginary part of the wavenumber is large enough to neglect the real part. The wavefield, dominated by conduction currents, is thus purely diffusive. This is the case of all the other geophysical electromagnetic methods (CSEM, MT, airborne EM). In the intermediate frequency range, both real and imaginary parts have a significant influence and can not be neglected. It is possible to define a ratio between displacement and conduction currents:

$$\eta = \frac{\varepsilon\omega}{\sigma}. \tag{3}$$

$\eta \gg 1$ indicates a mainly propagative regime. $\eta \ll 1$ indicates a mainly diffusive regime.

To solve the full frequency domain electromagnetic wave equation, equation 1 can be recast as a linear system and written in matricial form:

$$\mathbf{A}(\mu, \varepsilon, \sigma, \omega).\mathbf{h}(\omega) = \mathbf{b}(\omega). \tag{4}$$

$\mathbf{A}$ is the impedance matrix that include both the spatial and time derivative of the Helmoltz equation and the physical parameters describing the medium.
The wave equation is then discretized and solved using a finite-difference or finite-element method. In this paper, we use a Discontinious-Galerkin Finite-Element method (DG-FE). Boundary conditions are treated with PML layers (Berenger, 1994). A Dirichlet condition is also implemented at the extremity of the PML.

Such a system can be solved either using an iterative solver or a direct solver. The choice of one kind of solver or the other depends among other on the shape and the conditionning of the matrix $\mathbf{A}$. Furthermore, iterative solvers require much less memory than direct solvers than require analysis and factorization of the matrix $\mathbf{A}$. Direct solvers are in general more robust for numerically difficult cases such as in presence of strong contrasts or non-uniform grids. Direct solvers are interesting when many sources (many right-hand-side terms in 4) have to be used, because once the matrix $\mathbf{A}$ has been factorized, only inexpensive forward-backward substitution steps are necessary to compute the solutions for each source terms. In practive, following the initial idea of Pratt and Worthington (1990), almost all the forward modeling solver used for frequency-domain waveform inversion in seismic or GPR are direct solvers. However, because the conditionning of the matrix $\mathbf{A}$ depends also on the propagative/diffusive behavior of the wavefield, the choice of iterative or direct solver is still an open question. In particular, iterative solvers are easily preconditioned by the use of an a priori solution. In the case of EM waves in underground media, an efficient and accurate analytical or semi-analytical solution could be easily used as initial guess to speed up the convergence of iterative solvers.

In our work, the linear system 4 is solved efficently using the massively parallel direct solver MUMPS (Amestoy et al., 2000). MUMPS uses a multifrontal approach and is parallelized for distributed-memory architectures using the MPI standard. After the LU factorization of the matrix $\mathbf{A}$, the direct solution of the system to obtain magnetic field for various sources can be obtained with little additional computational effort by repeatidly using the same factorization (Pratt and Worthington, 1990).

In the following, all the tests are done in 2D. The modeling engine is based on a frequency-domain visco-acoustic/visco-elastic DG-FE code (Brossier et al., 2008; Brossier, 2011) initially developped for seismic waveform inversion. Obviously, extension to 2.5D or

3D will be necessary to process the real EM data in the intermediate frequency range. Stable schemes for 2.D helmoltz equation in the frequency domain exist (Song and Williamson, 1995), and the extension of the present work to other dimensions will just require to pay attention to the computational cost and solution accuracy in this specific frequency range. But this is out of the scope of the present study. For the 2D case presented here, all the computations run on single node of a small test cluster using up to 12 cores with a maximum of 32GB available memory.

We choose here for the 2D scheme a transverse electric (TE) configuration, that is with the eletric field polarized in the direction normal to the modeling plane and the magnetic field polarized in the modeling plane. The source is a magnetic dipole oriented in an arbitrary direction (x,z). Both real and imaginary parts of the vertical (z) and horizontal (x) components of the magnetic wavefield are computed, and corresponding values at each receiver positions are extracted using an apropriate interpolation.

Even though the modeling engine we use was developped for propagative wave purpose, the diffusive behavior is also well taken into account through the attenuation part (imaginary part of k) within the frequency domain approach. The PML layer acts as an attenuating layer in the propagative regime to avoid reflections at the edges of the model. In the diffusive regime, the PML layers reinforce the natural attenuation of the wavefield and has proved very efficient as long as they are greater than the half wavelength. However, the sources and receivers should preferably be located relatively far from PML to maintain a good modeling accuracy.

The figures 1, 2, 3, 4, 5 and 6 show respectively the modulus and phase of the vertical and horizontal magnetic field computed in the 6 configurations listed bellow, as well as the corresponding error maps. The modulus and phase error maps are respectively the absolute difference of the logarithm of the modulus and the phases between numerical and 2D analytical solutions. Expression of the 2D analytical solution used are given in Annexe B. The 6 configurations tested are:

1. Homogeneous medium with caracteristics of air: ε_r =1, μ_r =1 and $\rho = \infty$ at 5 MHz ($\eta \gg 1$).
2. Homogeneous medium with ε_r =10, μ_r =1 and ρ =1000 at 5 MHz ($\eta \sim 1$).
3. Homogeneous medium with ε_r =80, μ_r =1 and ρ =10 at 1 MHz ($\eta \ll 1$).
4. Homogeneous medium with ε_r =80, μ_r =1 and ρ =10 at 100 kHz ($\eta \ll 1$).
5. Homogeneous medium with ε_r =80, μ_r =1 and ρ =1 at 10 kHz ($\eta \ll 1$).
6. Homogeneous medium with ε_r =80, μ_r =1 and ρ =1 at 2.5 kHz ($\eta \ll 1$).

In this example, for the 6 configurations, the medium is of 80 m by 80 m, with 20 m width PML layers on each side. The average size of the grid cells is 0.3 m. A vertical magnetic dipole source is located at $x = 20m$ and $z = 20m$.

On the 6 figures, we clearly see that the PML are perfectly efficient at those frequencies to attenuate the wavefield and prevent any reflection event on the boundary and does

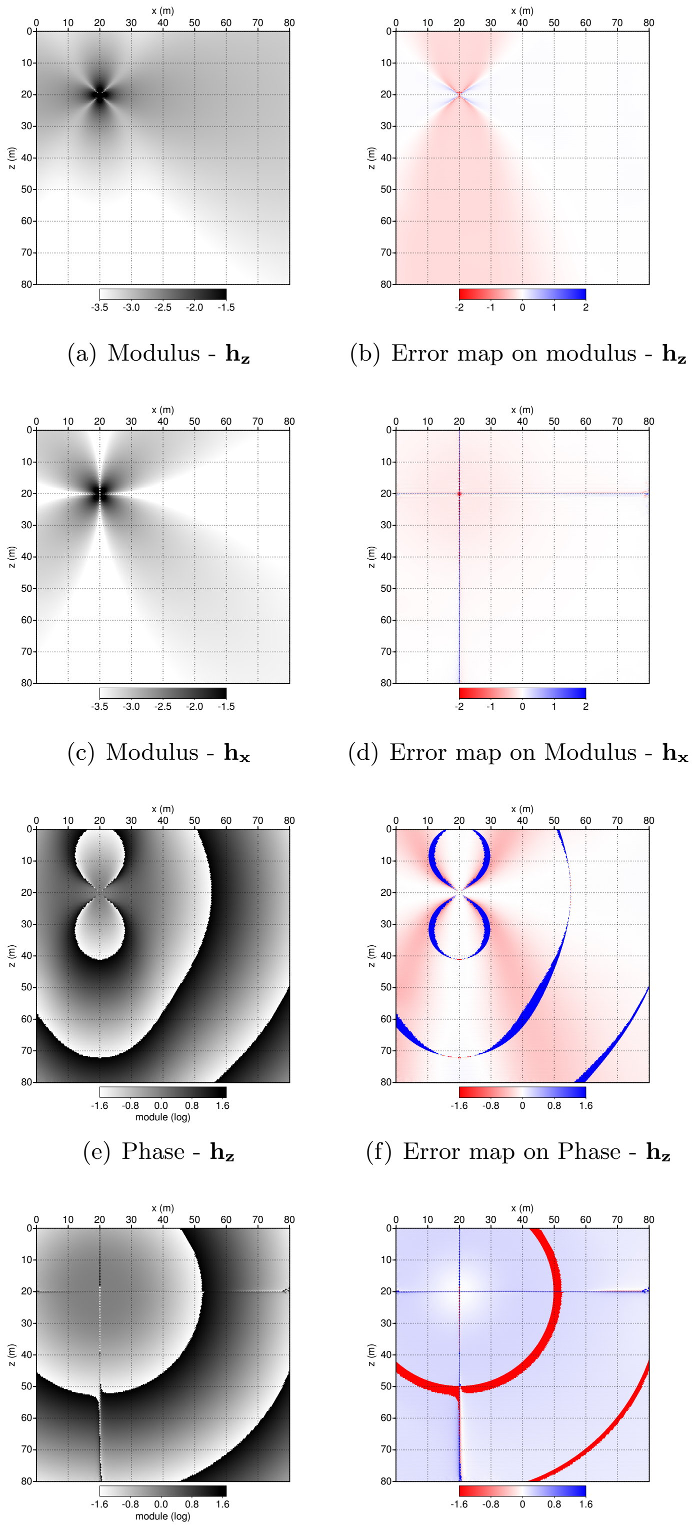

(a) Modulus - $\mathbf{h_z}$ (b) Error map on modulus - $\mathbf{h_z}$

(c) Modulus - $\mathbf{h_x}$ (d) Error map on Modulus - $\mathbf{h_x}$

(e) Phase - $\mathbf{h_z}$ (f) Error map on Phase - $\mathbf{h_z}$

(g) Phase - $\mathbf{h_x}$ (h) Error map on Phase - $\mathbf{h_x}$

Figure 1: Modulus and phase of the vertical and horizontal components of the magnetic field in air, and associated error maps. ε_r =1, μ_r =1 and $\rho = \infty$ at 5 MHz ($\eta \gg 1$). The wavefield is dominated by displacement currents and is purely propagative. The wavelength is about $\lambda \approx 60m$ and skin depth is $\delta_r = \inf$. The area outside the red square corresponds to the PML layer.

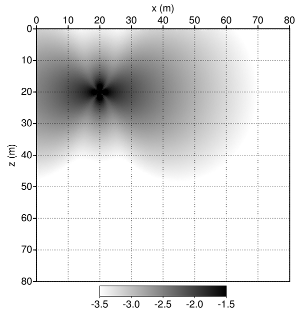

(a) Modulus - $\mathbf{h_z}$

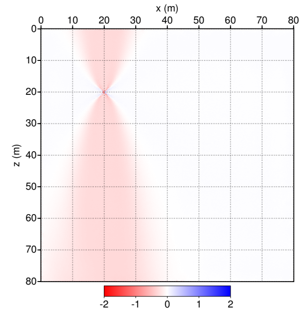

(b) Error map on modulus - $\mathbf{h_z}$

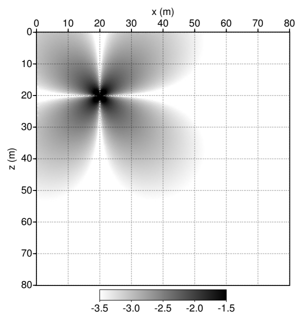

(c) Modulus - $\mathbf{h_x}$

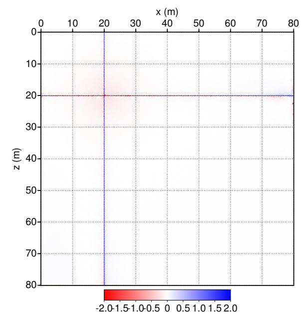

(d) Error map on Modulus - $\mathbf{h_x}$

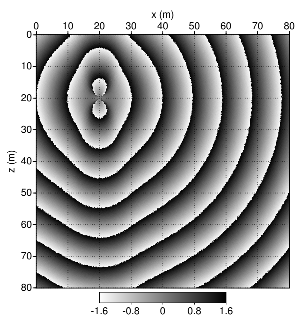

(e) Phase - $\mathbf{h_z}$

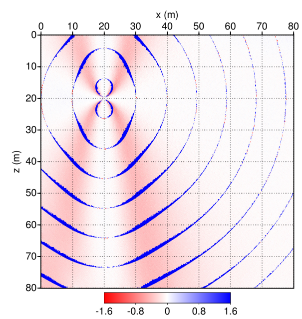

(f) Error map on Phase - $\mathbf{h_z}$

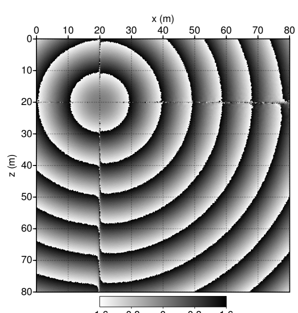

(g) Phase - $\mathbf{h_x}$

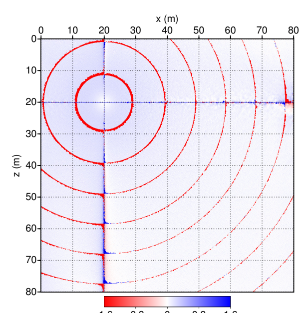

(h) Error map on Phase - $\mathbf{h_x}$

Figure 2: Modulus and phase of the vertical and horizontal components of the magnetic field in the first medium, and associated error maps. ε_r =10, μ_r =1 and ρ =1000 at 5 MHz ($\eta = 2.8$). The wavefield is dominated by displacement currents. The wavelength is about $\lambda \approx 19m$. The skin depth is $\delta \approx 17m$. The transition distance is $\tau \approx 3m$. The area outside the red square corresponds to the PML layer.

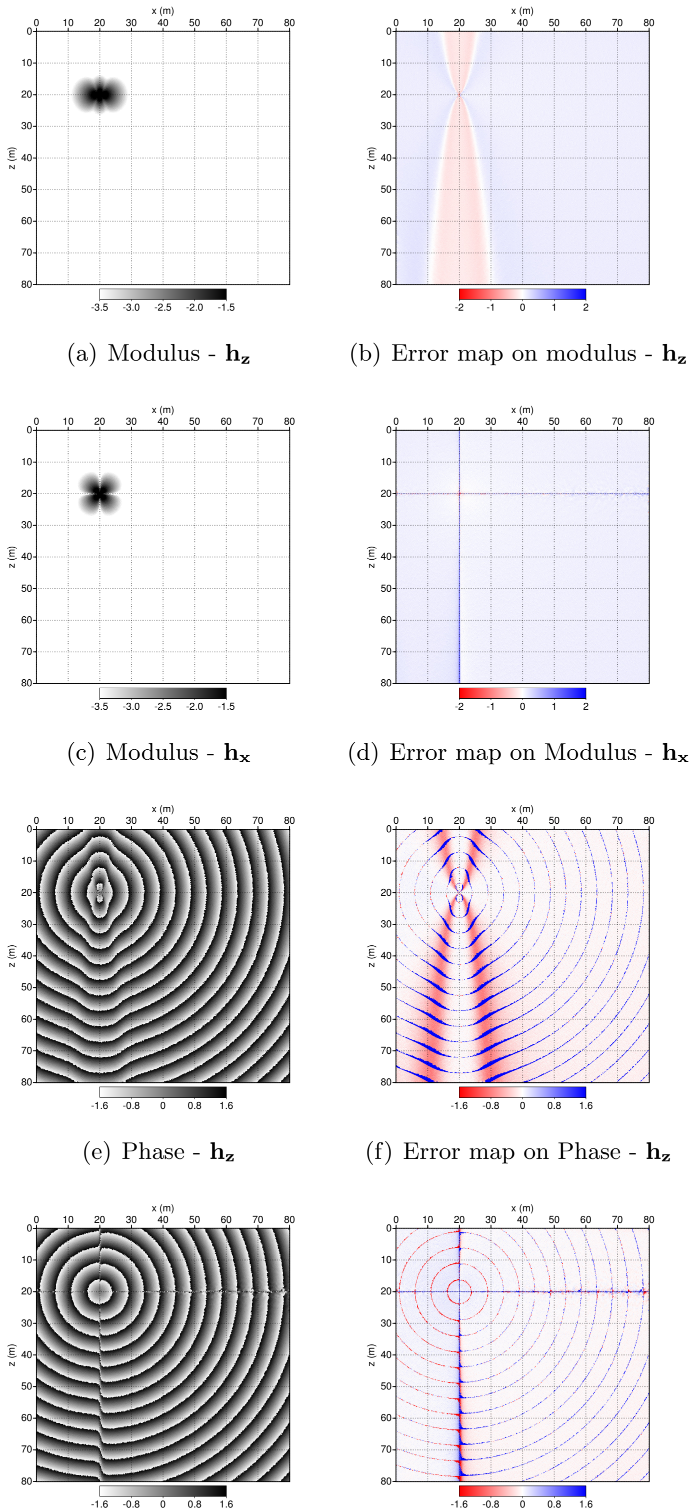

(a) Modulus - $\mathbf{h_z}$ (b) Error map on modulus - $\mathbf{h_z}$

(c) Modulus - $\mathbf{h_x}$ (d) Error map on Modulus - $\mathbf{h_x}$

(e) Phase - $\mathbf{h_z}$ (f) Error map on Phase - $\mathbf{h_z}$

(g) Phase - $\mathbf{h_x}$ (h) Error map on Phase - $\mathbf{h_x}$

Figure 3: Modulus and phase of the vertical and horizontal components of the magnetic field in the second medium, and associated error maps. ε_r =80, μ_r =1 and ρ =10 at 1 MHz ($\eta = 0.045$). The wavefield is dominated by conduction currents. The wavelength is about $\lambda \approx 10m$. The skin depth is $\delta \approx 1.6m$. The transition distance is $\tau \approx 1.1m$. The area outside the red square corresponds to the PML layer.

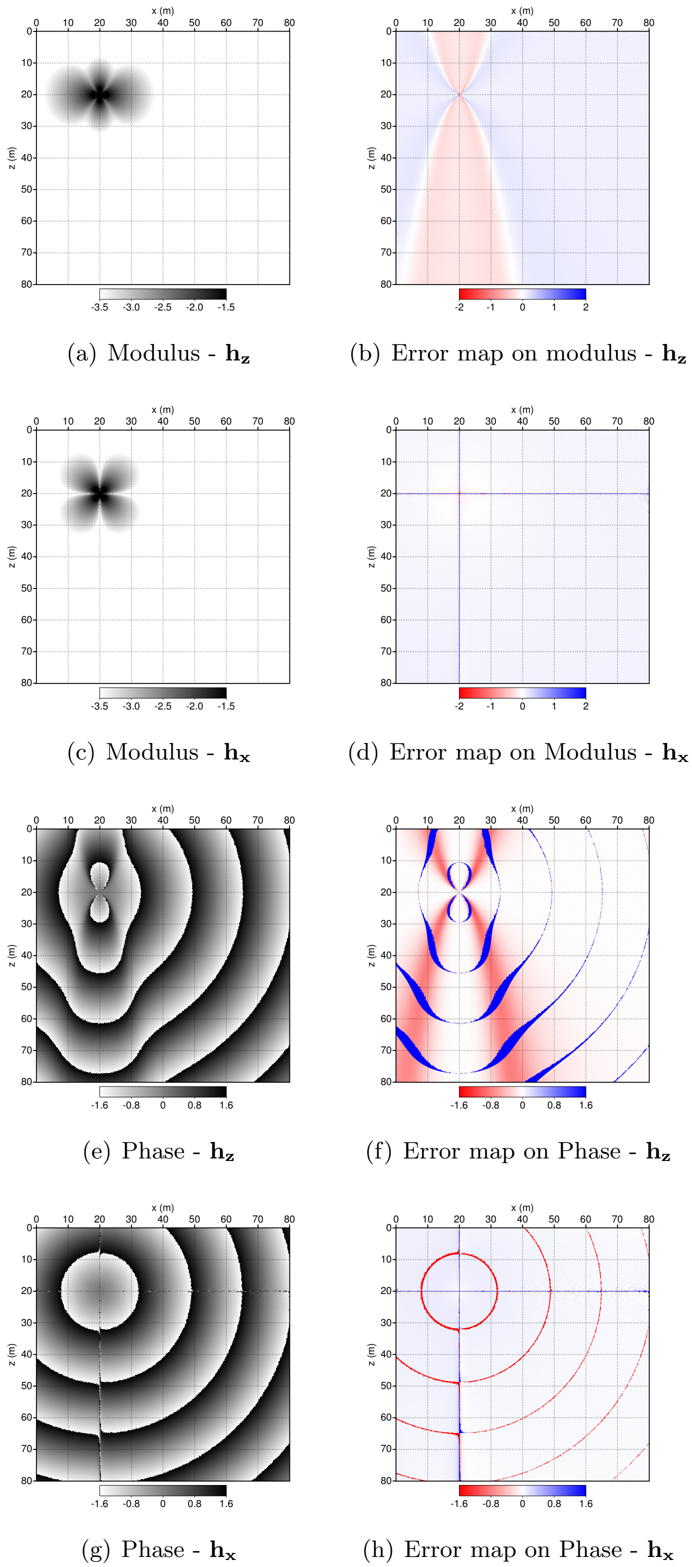

(a) Modulus - $\mathbf{h_z}$ (b) Error map on modulus - $\mathbf{h_z}$

(c) Modulus - $\mathbf{h_x}$ (d) Error map on Modulus - $\mathbf{h_x}$

(e) Phase - $\mathbf{h_z}$ (f) Error map on Phase - $\mathbf{h_z}$

(g) Phase - $\mathbf{h_x}$ (h) Error map on Phase - $\mathbf{h_x}$

Figure 4: Modulus and phase of the vertical and horizontal components of the magnetic field in the third medium, and associated error maps. ε_r =80, μ_r =1 and ρ =10 at 100 kHz ($\eta = 0.0045$). The wavefield is dominated by conduction currents. The wavelength is about $\lambda \approx 31.5m$. The skin depth is $\delta \approx 5.m$. The transition distance is $\tau \approx 3.5m$. The area outside the red square corresponds to the PML layer.

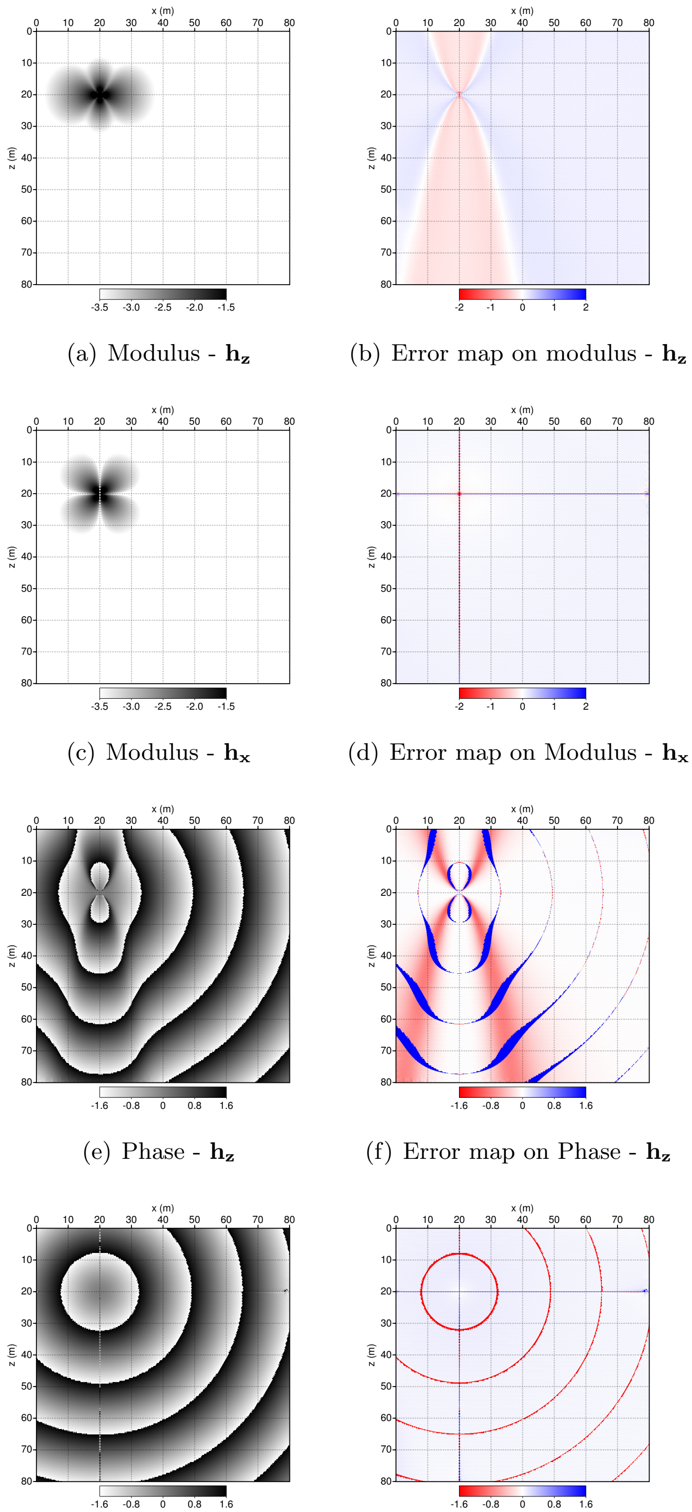

(a) Modulus - $\mathbf{h_z}$ (b) Error map on modulus - $\mathbf{h_z}$

(c) Modulus - $\mathbf{h_x}$ (d) Error map on Modulus - $\mathbf{h_x}$

(e) Phase - $\mathbf{h_z}$ (f) Error map on Phase - $\mathbf{h_z}$

(g) Phase - $\mathbf{h_x}$ (h) Error map on Phase - $\mathbf{h_x}$

Figure 5: Modulus and phase of the vertical and horizontal components of the magnetic field in the fourth medium and associated error maps. ε_r =80, μ_r =1 and ρ =1 at 10 kHz (η = 0.000045). The wavefield is dominated by conduction currents. The wavelength is about $\lambda \approx 31.5m$. The skin depth is $\delta \approx 5.m$. The transition distance is $\tau \approx 3.5m$. The area outside the red square corresponds to the PML layer.

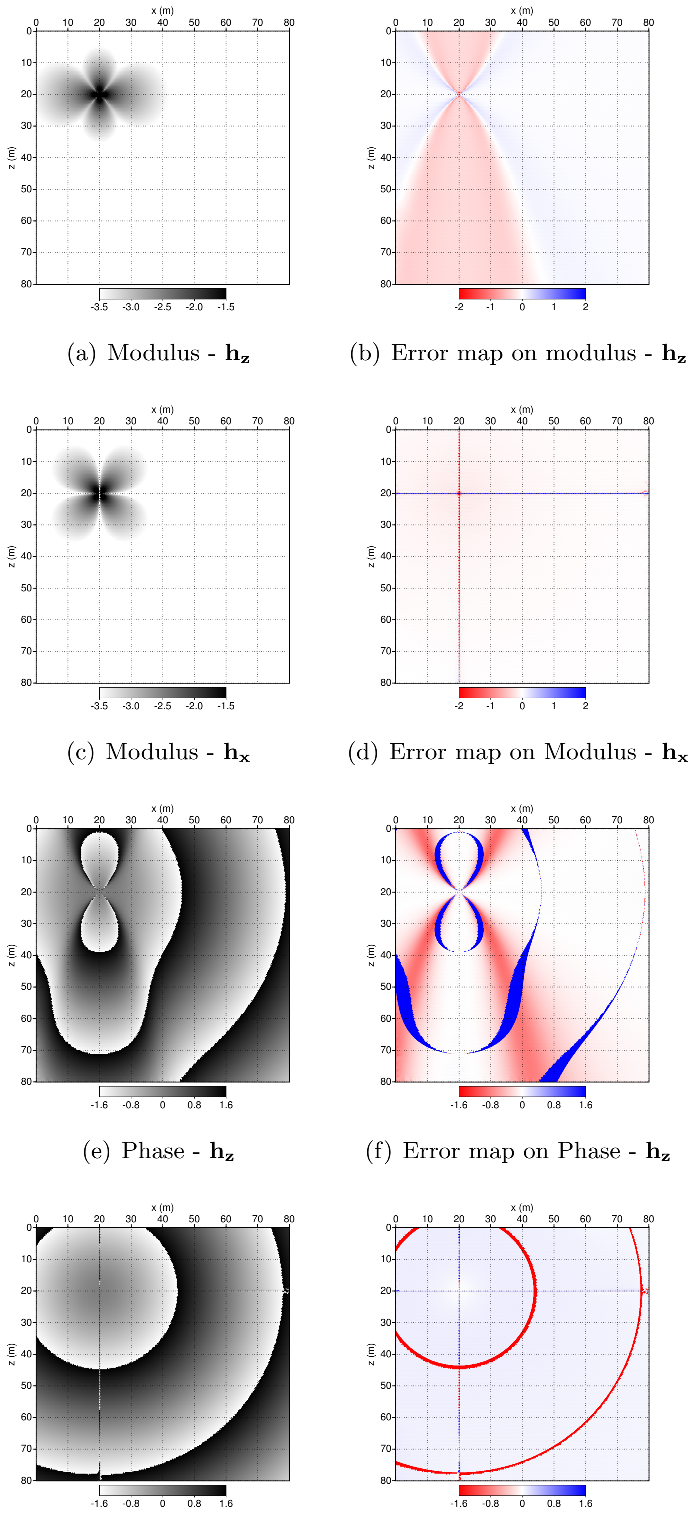

(a) Modulus - $\mathbf{h_z}$

(b) Error map on modulus - $\mathbf{h_z}$

(c) Modulus - $\mathbf{h_x}$

(d) Error map on Modulus - $\mathbf{h_x}$

(e) Phase - $\mathbf{h_z}$

(f) Error map on Phase - $\mathbf{h_z}$

(g) Phase - $\mathbf{h_x}$

(h) Error map on Phase - $\mathbf{h_x}$

Figure 6: Modulus and phase of the vertical and horizontal components of the magnetic field in the fifth medium, and associated error maps. ε_r =80, μ_r =1 and ρ =1 at 2.5 kHz (η = 0.000011). The wavefield is dominated by conduction currents. The wavelength is about $\lambda \approx 63m$. The skin depth is $\delta \approx 10m$. The transition distance is $\tau \approx 7m$. The area outside the red square corresponds to the PML layer.

not affect significantly the modulus and phase of the magnetic field inside the considered domain. The wavelength increases with decreasing frequencies, increasing resistivity, or decreasing permittivity. Configurations with largest wavelengths would require largest PML layers. However, when the conductivity is high (low resistivity), the wavefield is dramaticaly attenuated, which explain that smaller PML layers can also provide stable and accurate numerical solutions. Considering excitation with the verical magnetic dipole, the horizontal component of the magnetic field $\mathbf{h_x}$ is accurate both in phase and in amplitude in all directions. The vertical component $\mathbf{h_z}$ shows an anisotropic pattern of accuracy. Amplitude are very accurate in the direction normal to the direction of the dipole, and error is maximum in the axis of the dipole. Maximum error for the phase is at 45 from the horizontal and vertical axis. Those errors seems to originate from the source position. More accurate solutions would be obtained by better source implementation. A possibilty would be to use a field decomposition and solve the primary field with a semi-analytical solver and solve numerically the system for the secondary field only as done in Streich (2009) and Streich et al. (2011). But this in out of the scope of this study and the present accuracy is succificent to investigate the potential of 2D multiparameter EM wave-equation inversion.

Building the gradient and Hessian of the misfit function

The inverse problem associated to EM wave propagation in 2D or 3D heterogeneous medium involves many inverted parameters. The large amount of parameters and the computational cost required to solve each forward problem prevents from the use of a global optimization approach. The inversion approach proposed in this paper is in fact very similar the one use for seismic waveform inversion in the frequency domain (Pratt and Worthington, 1990; Virieux and Operto, 2009) and had also been tackled for GPR data at higher frequencies. For that we define for a given frequency ω the misfit function:

$$\mathcal{C}(\mathbf{m}) = \frac{1}{2}\sum_{s}^{N_s}\sum_{r}^{N_r}\left[(d_{cal_{s,r}} - d_{obs_{s,r}})^* S^*_{s,r} S_{s,r}(d_{cal_{s,r}} - d_{obs_{s,r}})\right] \tag{5}$$

with $\mathbf{m}$ the vector of inverted model parameters, N_s and N_r the number of sources and receivers, $S_{s,r}$ a weighting function associated to the data covariance, and $d_{obs_{s,r}}$ the observed complex data for the source-receiver pair $s-r$. * denotes the complex conjugate.
The calculated data is obtained by:

$$d_{cal_{s,r}} = \mathcal{P}_{s,r}\mathbf{h_s} \tag{6}$$

where $\mathbf{h_s}$ is the magnetic field vector (including all components) for the source s and $\mathcal{P}_{s,r}$ is a restriction operator used to extract the values of the wavefield $\mathbf{h_s}$ at the position of the receiver r. $\mathbf{h_s}$ is the solution of the wave equation given previously:

$$\mathbf{A}(\mathbf{m}).\mathbf{h_s} = \mathbf{b_s}. \tag{7}$$

Tomographic imaging is usually done by linearized inversion, thus the model $\mathbf{m_{k+1}}$ is improved iteratively following the recurrence: from an initial guess $\mathbf{m_0}$, a sequence $\mathbf{m_k}$ is computed such that:

$$\mathbf{m_{k+1}} = \mathbf{m_k} \; + \; \alpha_k \Delta\mathbf{m}. \tag{8}$$

This requires the computation of the model update $\mathbf{\Delta m}$ at each iteration k, and to perform a line search to determine the steplength α_k.

The model update is often computed in the framework of the Gauss-Newton approximation that requires the explicit computation of the Fréchet derivative matrix $\mathbf{J}$. The model update is obtained by solving the Gauss-Newton equation for instance using a LSQR algorithm (Paige and Saunders, 1982a,b):

$$\left[\mathbf{J}^t\,\mathbf{J}\right]\mathbf{\Delta m} \;=\; \mathbf{J}^t\,\mathbf{\Delta d}, \tag{9}$$

where $\mathbf{\Delta d}$ is the data residual vector.

However, when the number of inverted parameter is large, computing explicitely the Fréchet derivative matrix becomes prohibitive. A more appropriate approach consists in computing only the gradient of the misfit function $\boldsymbol{\gamma}(\mathbf{m}) = \mathbf{J}^t\,\mathbf{\Delta d}$ using a matrix-free method such as the adjoint-state method. Then the influence of the Hessian in the inversion can be obtained by a quasi-Newton optimization algorithm such as l-BFGS (Nocedal and Wright, 1999) that efficienty estimate the inverse Hessian $\mathbf{Q_k}$ from former values of the gradient. The l-BFGS algorithm does not require any additional computation, but only requires to store the 'l' previous gradients and is thus very efficient. The model is then updated as follow:

$$\mathbf{m_{k+1}} = \mathbf{m_k} \;-\; \alpha_k \mathbf{Q_k}\boldsymbol{\gamma_k}(\mathbf{m}). \tag{10}$$

To derive the expression of the gradient of the misfit function, we use the adjoint-state formalism (Plessix, 2006). We define for that the Lagrangian, that is a new functional augmented with constrains associated with the state equations, and we introduced the adjoint variables $\lambda_{s,r}$ (one scalar for each source-receiver pair) and $\boldsymbol{\mu_s}$ (one vector for each source):

$$\begin{aligned}\mathcal{L}(\mathbf{m}) \quad = \Re\Bigg\{ \quad & \frac{1}{2}\sum_s^{N_s}\sum_r^{N_r}\left[(d_{cal_{s,r}} - d_{obs_{s,r}})^* S^*_{s,r} S_{s,r}(d_{cal_{s,r}} - d_{obs_{s,r}})\right] \\ & - \sum_s^{N_s}\sum_r^{N_r}\lambda_{s,r}\left(d_{cal_{s,r}} - \mathcal{P}_{s,r}\mathbf{h_s}\right) \\ & - \sum_s^{N_s}\langle\boldsymbol{\mu_s}\,,\;\mathbf{A}(\mathbf{m}).\mathbf{h_s} - \mathbf{b_s}\rangle \quad \Bigg\}\end{aligned} \tag{11}$$

The derivative of $\mathcal{L}(\mathbf{m})$ with respect to the model parameters gives the gradient of the misfit function:

$$\boldsymbol{\gamma}(\mathbf{m}) = \frac{\partial\mathcal{L}(\mathbf{m})}{\partial\mathbf{m}} = \Re\Bigg\{\sum_s^{N_s}\left(\boldsymbol{\mu_s}^*\frac{\partial\mathbf{A}}{\partial\mathbf{m}}\mathbf{h_s}\right)\Bigg\} \tag{12}$$

The adjoint states $\boldsymbol{\mu_s}$ and $\lambda_{s,r}$ are defined repectively by $\frac{\partial\mathcal{L}}{\partial\mathbf{h_s}} = 0$ and $\frac{\partial\mathcal{L}}{\partial d_{cal_{s,r}}} = 0$, that gives:

$$\frac{\partial\mathcal{L}}{\partial d_{cal_{s,r}}} = 0 = S^*_{s,r}S_{s,r}\left(d_{cal_{s,r}} - d_{obs_{s,r}}\right) \;-\; \lambda_{s,r} \tag{13}$$

and

$$\frac{\partial \mathcal{L}}{\partial \mathbf{h_s}} = 0 = \sum_{r}^{N_r} \mathcal{P}^{*}_{s,r} \lambda_{s,r} \quad - \quad \mathbf{A}^{*} \boldsymbol{\mu_s}. \tag{14}$$

We can deduce that the adjoint wavefield $\boldsymbol{\mu_s}$ is obtained by solving the linear system:

$$\mathbf{A}^{*} \boldsymbol{\mu_s} \quad = \quad \sum_{r}^{N_r} \mathcal{P}^{*}_{s,r} S^{*}_{s,r} S_{s,r} \left(d_{cal_{s,r}} - d_{obs_{s,r}} \right). \tag{15}$$

This system is similar to the system 7 but taking the conjugate of the impedance matrix $\mathbf{A}$ and with the data residuals as a source term. That means that the ajdoint field is obtained by propagating simultaneously and backward in time all the data residuals. Then the gradient of the misfit function for a given frequency is the sum over sources of the correlation of the forward fields $\mathbf{h_s}$ with the backpropagated fields $\boldsymbol{\mu_s}$, and weighted by the diffraction matrix $\frac{\partial \mathbf{A}}{\partial \mathbf{m}}$. The diffraction matrix depends on the chosen parameterization. It provides the diffraction pattern of the imaged parameter. For instance, if we take a natural parameterization such as the logarithm of conductivity ($L_\sigma = \ln \sigma_r$), relative permittivity ($L_{\varepsilon_r} = \ln \varepsilon_r$), and relative permeabiliy ($L_{\mu_r} = \ln \mu_r$) are inverted, the diffraction matrices are simply:

$$\frac{\partial \mathbf{A}}{\partial L_\sigma} \quad = \quad -i\mu\sigma\omega \tag{16}$$

$$\frac{\partial \mathbf{A}}{\partial L_{\varepsilon_r}} \quad = \quad \mu\varepsilon\omega^2 \tag{17}$$

$$\frac{\partial \mathbf{A}}{\partial L_{\mu_r}} \quad = \quad \mu\varepsilon\omega^2 - i\mu\sigma\omega \tag{18}$$

Otherwise, if a direct parameterization in conductivity (σ), relative permittivity (ε_r), and relative permeabiliy (μ_r) is chosen, the diffraction matrices are:

$$\frac{\partial \mathbf{A}}{\partial \sigma} \quad = \quad -i\mu\omega \tag{19}$$

$$\frac{\partial \mathbf{A}}{\partial \varepsilon_r} \quad = \quad \mu\varepsilon_0\omega^2 \tag{20}$$

$$\frac{\partial \mathbf{A}}{\partial \mu_r} \quad = \quad \mu_0\varepsilon\omega^2 - i\mu_0\sigma\omega. \tag{21}$$

Validation of the gradient

Monoparameter inversion

A small synthetic model has been used to validate the gradients of the misfit function for the various parameters: ε_r, σ, μ_r, and the logarithm of the 2 first parameters ($L_\sigma = \ln \sigma_r$) and relative permittivity ($L_{\varepsilon_r} = \ln \varepsilon_r$). The model is a 50 m by 90 m rectangle with 2 small square positive and negative anomalies. We use here a very favorable acquisition with sources and receivers that spread all around the model, providing data associated to electromagnetic field transmited through the anomalies, in a kind of cross-borehole configuration. The background model has $\varepsilon_r = 5$, $\rho = 250\ \Omega.m$ and $\mu_r = 1$. The starting model is the homogeneous background model. There is no air layer in this validation case, and the sources and receivers are punctual magnetic dipoles located directly in the background medium. In each case, the data are built using the same modeling algorithm than the one used for the inversion, and each parameter is considered independently (inversion of σ only from data with perurbation on σ only, etc.).

We present the gradients and inversion results for this test case for a single frequency 5 MHz figures 7, 8 and 9. In each figure, the gradient of the misfit function $\boldsymbol{\gamma(m)}$ gives the descent direction in the model space. The diagonal of the Hessian $diag\,(\mathbf{H}(\mathbf{m}))$ is used as a preconditionner to scale the descent direction. Its role is to scale the descent direction to be consistent with the physical dimension of the inverted parameter, by correcting the gradient from the spatial amplitude decrease of the electromagnetic wavefield and compensate the uncomplete illumination provided by the specific acquisition layout (Pratt et al., 1998). The model perturbation is simply the product $\mathbf{\Delta m} = (diag\,(\mathbf{H}(\mathbf{m})))^{-1}\ .\ \boldsymbol{\gamma(m)}$. Then a linesearch is necessary to determine a model parameter from this model perturbation. We cleary see for the 3 parameters that the accuracy of the reconstructed model, and in particular the resolution, are improved with iterations.

The 3 parameters are well reconstructed after a few tenth iterations. The conductivity is the parameter that is best reconstructed both in term of magnitude and resolution. In fact, the imaging resolution of ε_r depends on the acquisition survey and depends strongly on the frequency. In contrast, the resolution for the conductivity is more dependent on the acquisition geometry and less on the frequency. The permeability μ_r is less sensitive to the data and its resolution is lower than for the other parameters.

The figure 10 represents the misfit decrease for the 3 parameters. The speed of decrease is of the same order of magnitude for the 3 parameters, however slightly faster for ε_r and slower for μ_r. Furthermore, considering a same stoping criterion, the parameter σ is better explained with a decrease of the misfit of almost 4 orders of magnitude. In comparison, the misfit decreases of 3 orders of magnitude for ε_r and 2 orders of magnitudes for μ_r. This illustrate that at this frequency range, the conductivity is the most sensitive parameter, and the permeability is the less sensitive.

The results obtained using a parameterization in logarithm instead of the natural parameters are very similar, although the convergence is slightly faster with the logarithm.

Multiparameter inversion

The same test is performed then but for the simultanuous inversion of both conductivity and relative permittivity from data generated with both perturbation of conductivity and permittivity. The simultanuous inversion of several classes of parameters is more complicated because the solution is less unique. Especially in the case of electromagnetic waves at those frequencies, variations in conductivity and permittivity both can produce changes

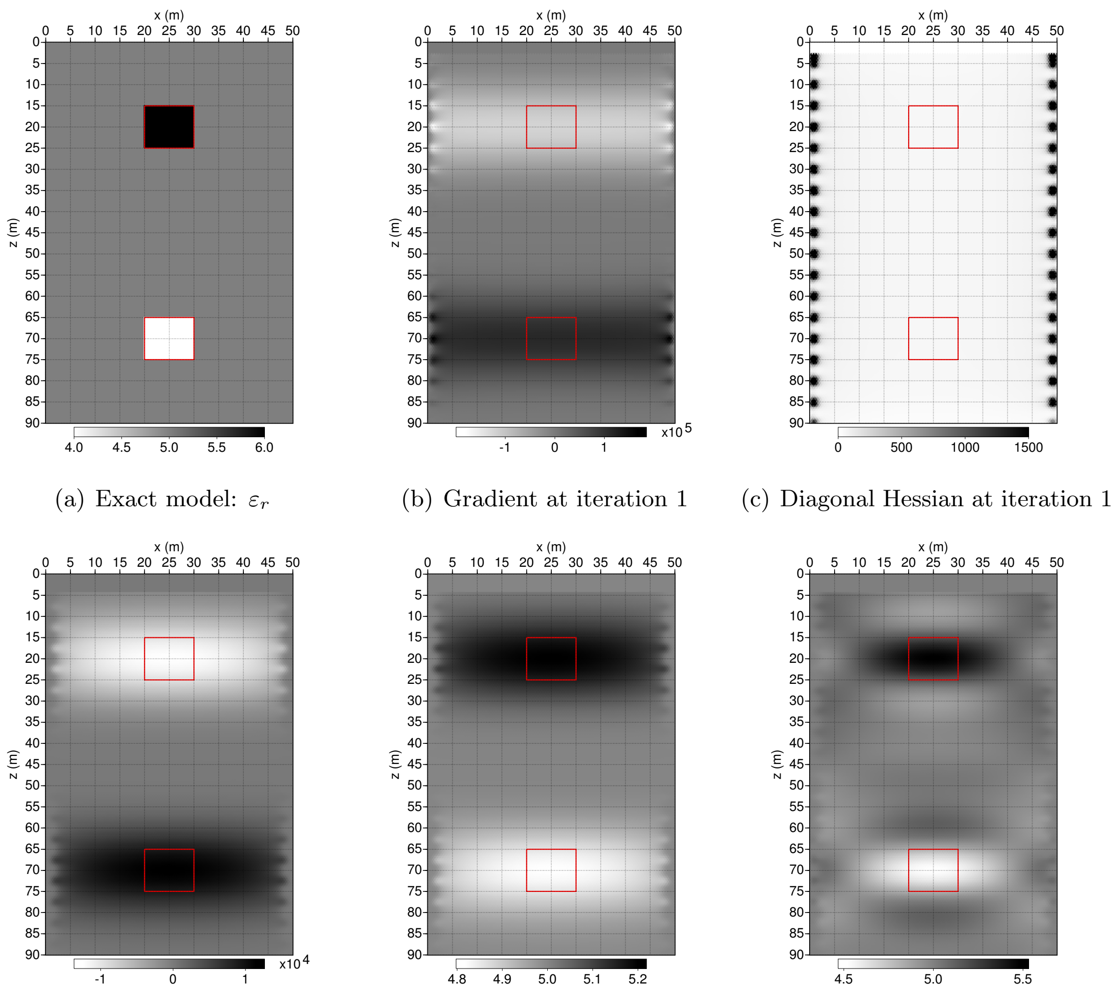

(a) Exact model: ε_r

(b) Gradient at iteration 1

(c) Diagonal Hessian at iteration 1

(d) Model perturbation at iteration 1

(e) Inverted model at iteration 1

(f) Final inverted model

Figure 7: Illustration of the reconstruction steps for the parameter ε_r: gradient $\boldsymbol{\gamma(\varepsilon_r)}$, diagonal of the Hessian $\mathbf{H}(\varepsilon_\mathbf{r})$, scaled descent direction $\boldsymbol{\Delta}\varepsilon_\mathbf{r}$, reconstructed permittivity model ε_r at iteration 1 and last iteration.

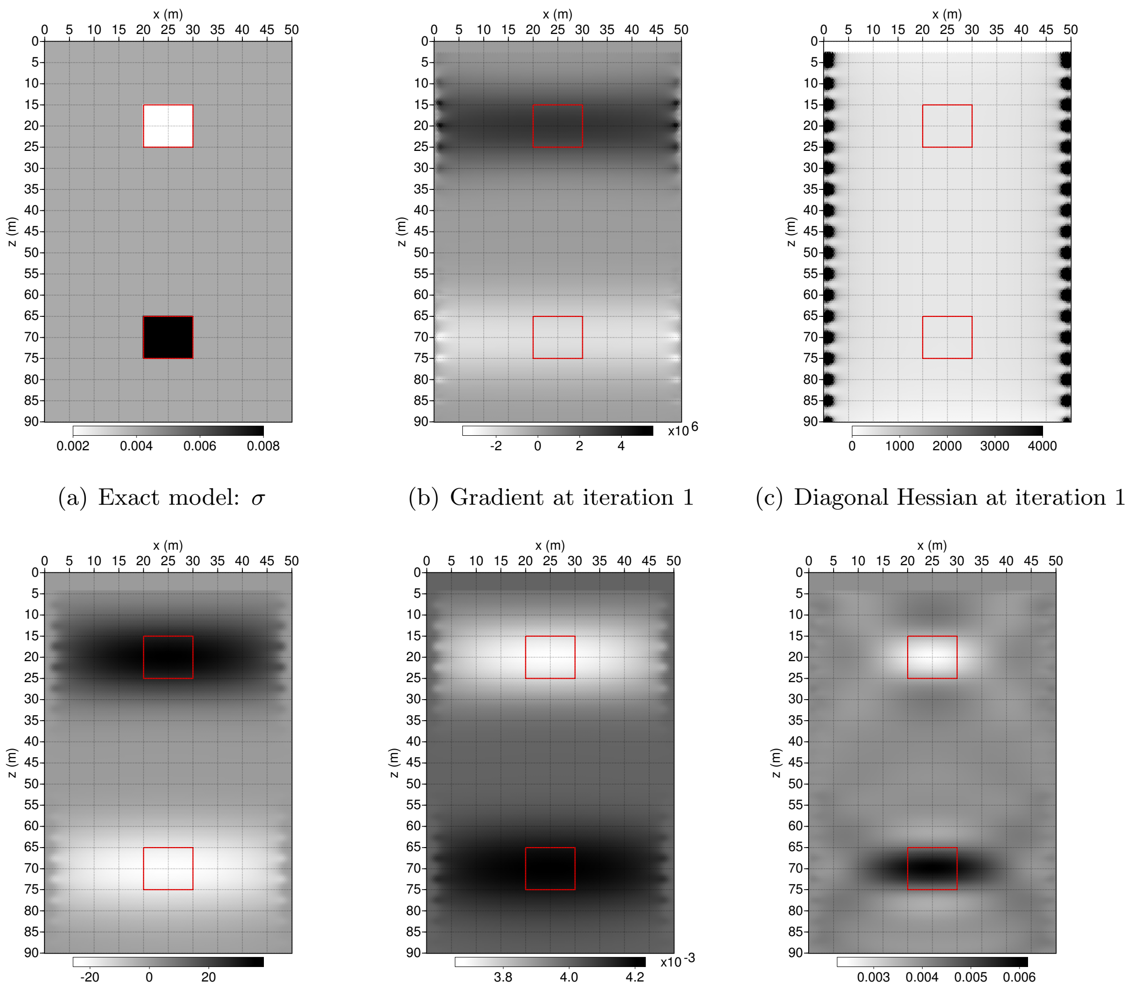

(a) Exact model: σ

(b) Gradient at iteration 1

(c) Diagonal Hessian at iteration 1

(d) Model perturbation at iteration 1

(e) Inverted model at iteration 1

(f) Final inverted model

Figure 8: Illustration of the reconstruction steps for the parameter σ: gradient $\boldsymbol{\gamma}(\boldsymbol{\sigma})$, diagonal of the Hessian $\mathbf{H}(\sigma)$, scaled descent direction $\boldsymbol{\Delta}\sigma$, reconstructed permittivity model σ at iteration 1 and last iteration.

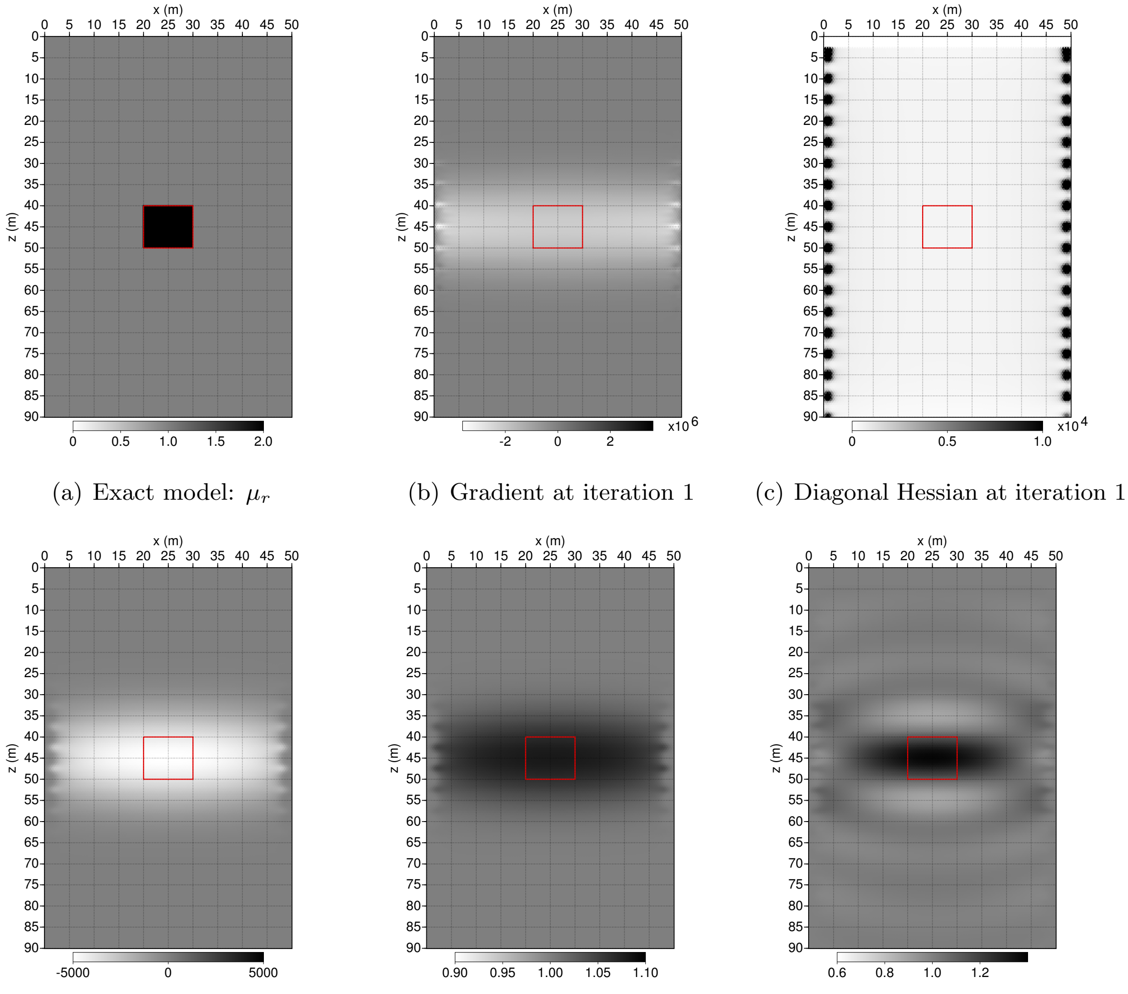

(a) Exact model: μ_r
(b) Gradient at iteration 1
(c) Diagonal Hessian at iteration 1
(d) Model perturbation at iteration 1
(e) Inverted model at iteration 1
(f) Final inverted model

Figure 9: Illustration of the reconstruction steps for the parameter μ_r: gradient $\boldsymbol{\gamma}(\boldsymbol{\mu_r})$, diagonal of the Hessian $\mathbf{H}(\mu_\mathbf{r})$, scaled descent direction $\boldsymbol{\Delta}\mu_\mathbf{r}$, reconstructed permeability model μ_r at iteration 1 and last iteration.

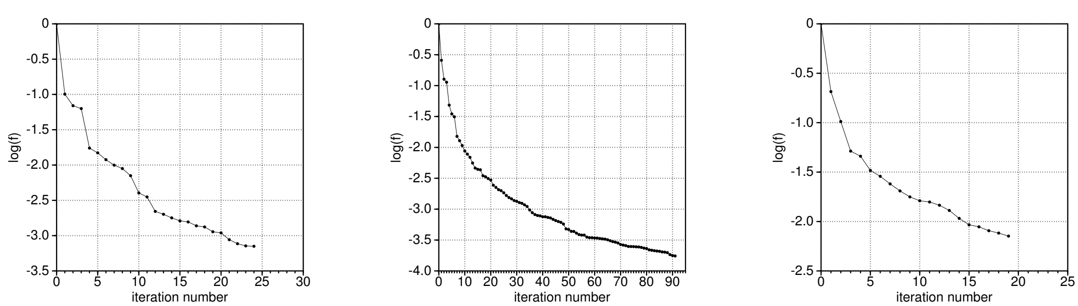

(a) Permittivity ε_r
(b) Conductivity σ
(c) Permeability μ_r

Figure 10: Misfit function decrease (in log) for the 3 parameters ε_r, σ and μ_r.

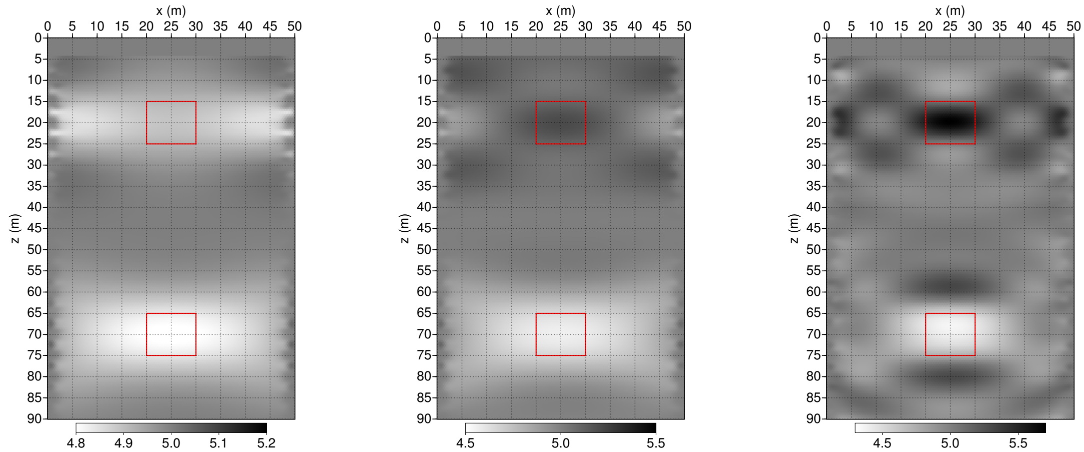

(a) Permittivity ε_r iteration 1 (b) Permittivity ε_r iteration 5 (c) Permittivity ε_r final iteration (33)

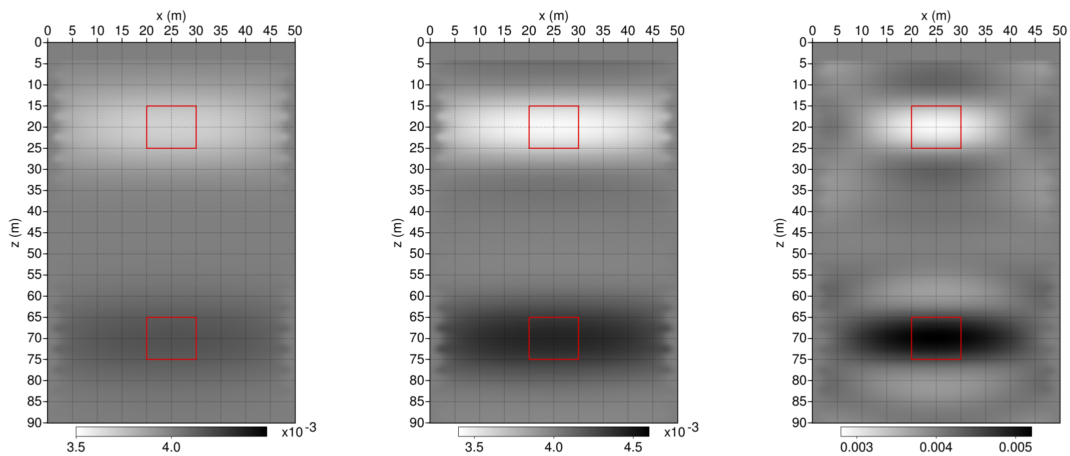

(d) Conductivity σ iteration 1 (e) Conductivity σ iteration 5 (f) Conductivity σ final iteration (33)

Figure 11: Simultaneous inversion of conductivity σ and relative permittivity ε_r.

in the phase of the signals in similar or opposite maner. However, the amplitude is mainly driven by the conductivity (the imaginary part of the wavenumber controls the attenuation), so we can expect the inversion of the conductivity to be more linear, and thus its reconstruction to be more stable than the reconstruction of the permittivity. The Hessian plays a role in mitigating the tradeoff between the parameters. However the exact Hessian is to expensive to be computed. In our approach, the diagonal of the Hessian is computed at the first iteration and kept during the inversion. The off-diagonal terms are estimated in a finite-difference sense from former values of the gradients. This estimation is not perfect and could be improved for instance by using the Truncated Newton approach proposed by (Metivier et al., 2014). However, we show it is sufficient in this 2 parameters-case.

Intermediar and final inversion results are presented figure 11. The conductivity model is progressively reconstructed through iterations. The final result is almost similar to the one obtained in monoparameter inversion. On the other hand, the permittivity model at first iterations is updated in the wrong way, especially for the upper anomaly. This is due to the tradeoff between the 2 parameters. That means that inversion tries to explain with permittivity variations a perturbation in the data that is due to the conductivity. After a few iterations, the conductivity is better imaged, then the permittivity is updated in the good way. Artefacts that remains in the final reconstructed image of ε_r are due to this tradeoff.

This conclusion is crucial. Obviously, this tradeoff may be less critical depending of the frequency of investigation, and would be probably mitigated by the simultanoues inversion of data at several frequencies. However, it highlights the relative robustness of the inversion of the conductivity and the high non-linearity associated to the inversion of the permittivity.

MODELING AND IMAGING WITH SURFACE-SURFACE ACQUISITION

Model description and numerical modeling

In the following part we perform a synthetic modeling and inversion test on more realistic surface-surface acquisition configuration. The investigated medium is homogeneous with resitivity $\rho = 100\,\Omega.m$ and relative permittivity $\varepsilon_r = 10$, and with two 5m * 5m square inclusions located at 5 m bellow the surface repectively with properties ($\rho = 10\,\Omega.m$, $\varepsilon_r = 100$) and ($\rho = 1000\,\Omega.m$, $\varepsilon_r = 1$). A 5 m air layer is added at the top of the model. Relative permeability is kept constant at μ_r =1 in the whole model. The sources are vertical magnetic dipoles spread every 5 m at 1 m above the surface. The receivers are bi-componant magnetic sensors ($h_x(x_r)$ and $h_z(x_r)$) also placed at 1 m above the surface but every 2.5 m. The exact model is depicted by figures 12 a and b. The figures 12-c and 12-d depict the starting model that will be used further for the inversion test.

We first study the behavior of the forward modeling engine in this configuration. Simulations are performed at 500 kHz, 2 MHz, 6 MHz and 12 MHz. The table 1 reminds the wavelengths, skin depth and transition distance in air and in the background medium for each of those frequencies. The modulus and phase of the 2 components of the magnetic fields are represented figures 13 to 16. We clearly see the perturbation of the magnetic field due to the heterogeneities at the frequencies. The figures 17 and 18 represent the modulus and phases of the differences between the magnetic fields with and without the 2 square heterogeneities for the lowest and the highest frequency. Those 2 figures highlight in fact the diffracted field generated by the 2 heterogeneities. The values of the diffracted field at the receiver positions correspond to what is the information we will have access for the inversion. It gives a first idea of what kind of imaging resolution we can expect for a single source in a noise-free context. We can deduce from those figures the importance of the design of the acquisition survey depending on the frequency of investigation. At low frequency, the information show a high spatial redundancy, but at the highest frequencies, a better spatial coverage is necessary to avoid phase ambiguity.

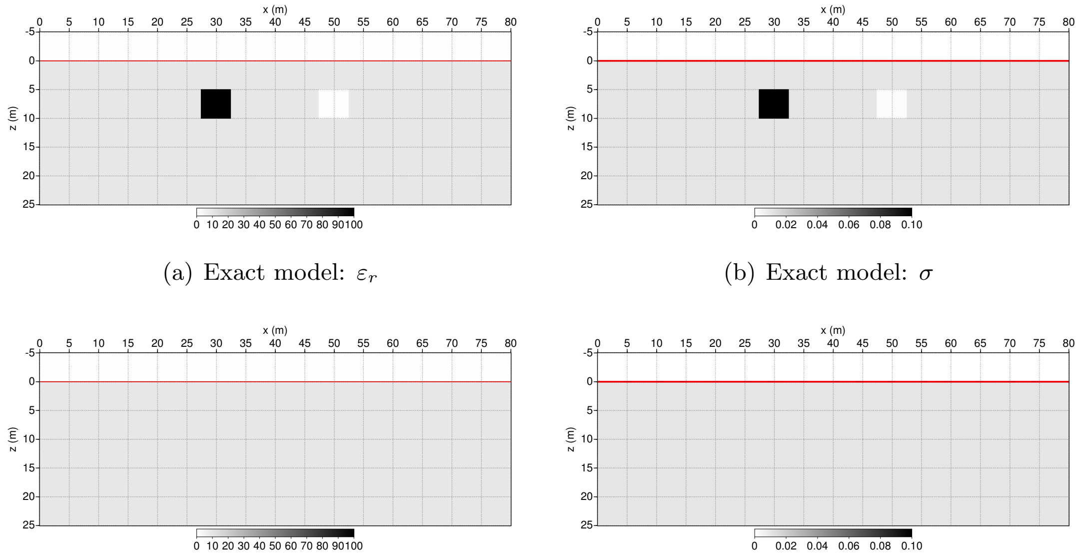

(a) Exact model: ε_r

(b) Exact model: σ

(c) Starting model: ε_r

(d) Starting model: σ

Figure 12: Permittivity and conductivity models used for the surface-surcace aquisition test. The red line depicts the air/soil boundary.

Inversion at a single fixed frequency

A first inversion test is performed independantly frequency by frequency. The ratio between wavelength and the size of the structures and the ratio between condution and displacement current being very different depending on the frequency, we expect very different behavior of the inversion for each frequency.

The final inversion result for the 2 parameters is shown figure 19, and the data misfit

	500 kHz	2MHz	6 MHz	12 MHz
λ_{air} (m)	500.	150.	50.	25.
$\lambda_{background}$ (m)	44.1	21.1	11.0	6.7
$\delta_{background}$ (m)	7.2	3.8	2.4	2.0
$\tau_{background}$ (m)	5.0	2.5	1.4	0.9
$\eta_{background}$	0.028	0.11	0.33	0.67

Table 1: Characteristics lengths of the wavefields at the 4 studied frequencies: wavelength in air and in the background medium ($\lambda = \frac{2\pi}{\Re(k)}$), skin depth $\delta = -\frac{1}{\Im(k)}$, transition distance $\tau = \frac{1}{|k|}$, ratio between condution currents and displacement currents $\eta = \frac{\varepsilon\omega}{\sigma}$.

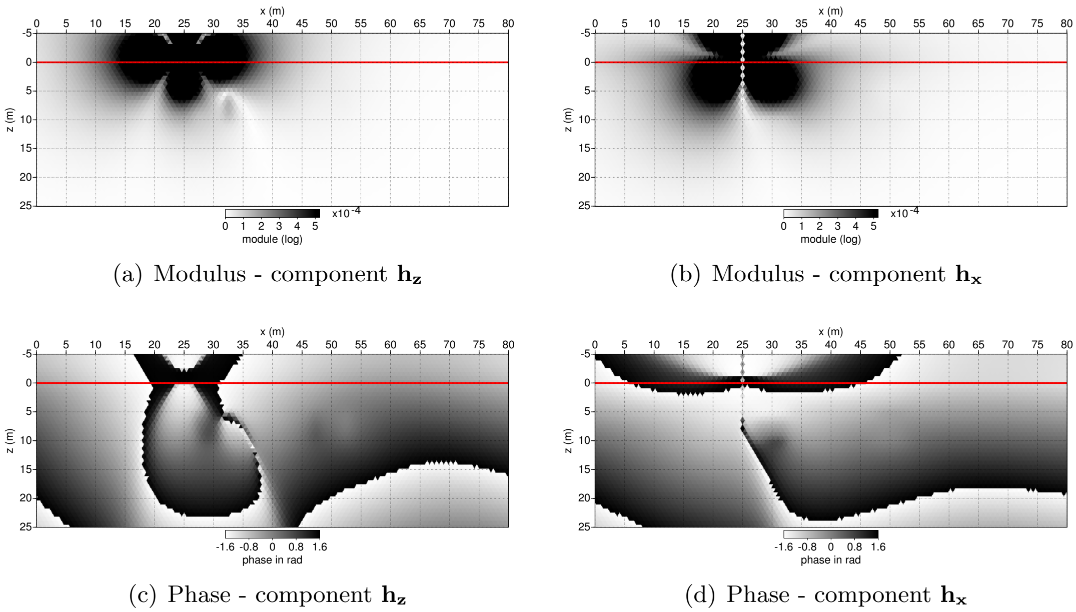

(a) Modulus - component $\mathbf{h_z}$

(b) Modulus - component $\mathbf{h_x}$

(c) Phase - component $\mathbf{h_z}$

(d) Phase - component $\mathbf{h_x}$

Figure 13: Modulus and phase of the vertical and horizontal components of the magnetic field $\mathbf{h_z}$ and $\mathbf{h_x}$ computed in the exact model of figure 12 at 500 kHz.

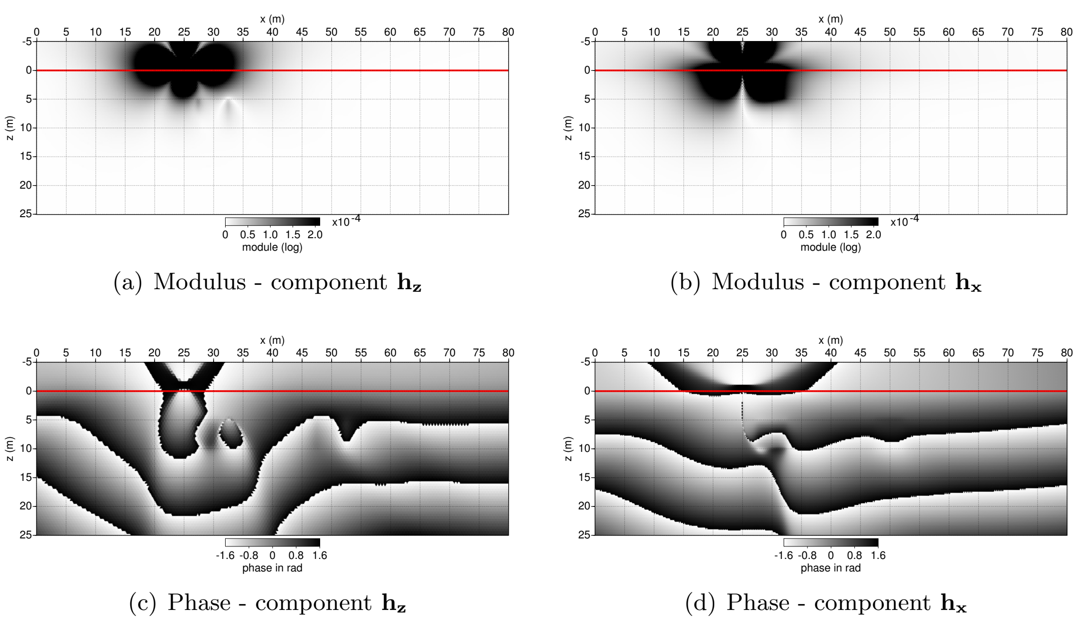

(a) Modulus - component $\mathbf{h_z}$

(b) Modulus - component $\mathbf{h_x}$

(c) Phase - component $\mathbf{h_z}$

(d) Phase - component $\mathbf{h_x}$

Figure 14: Modulus and phase of the vertical and horizontal components of the magnetic field $\mathbf{h_z}$ and $\mathbf{h_x}$ computed in the exact model of figure 12 at 2 MHz.

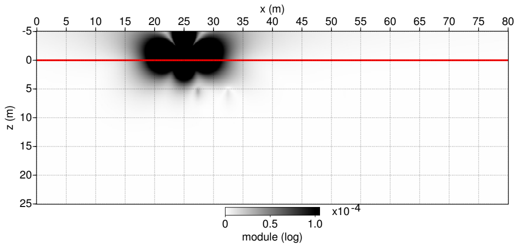

(a) Modulus - component $\mathbf{h_z}$

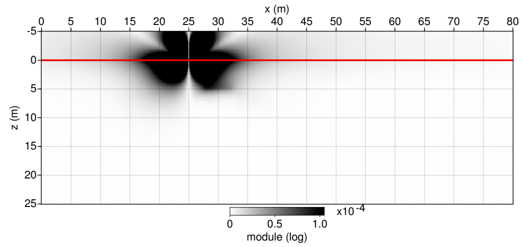

(b) Modulus - component $\mathbf{h_x}$

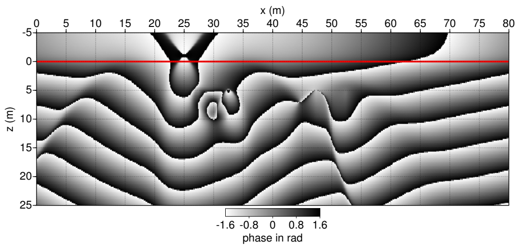

(c) Phase - component $\mathbf{h_z}$

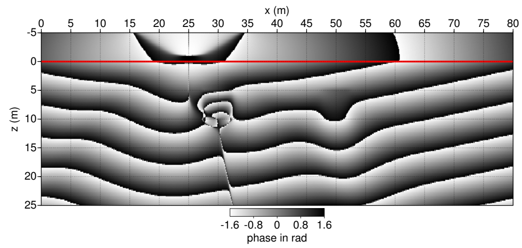

(d) Phase - component $\mathbf{h_x}$

Figure 15: Modulus and phase of the vertical and horizontal components of the magnetic field $\mathbf{h_z}$ and $\mathbf{h_x}$ computed in the exact model of figure 12 at 6 MHz.

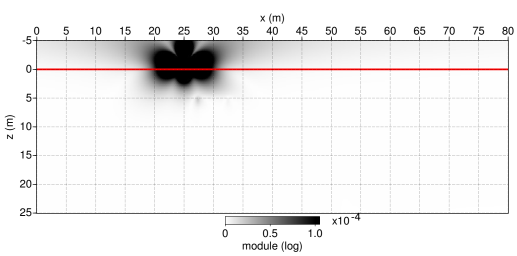

(a) Modulus - component $\mathbf{h_z}$

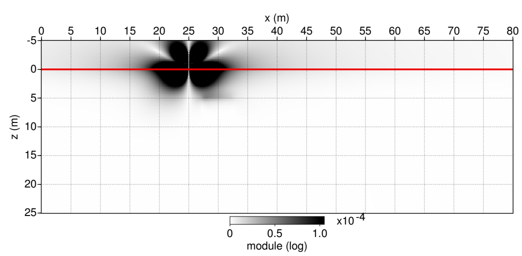

(b) Modulus - component $\mathbf{h_x}$

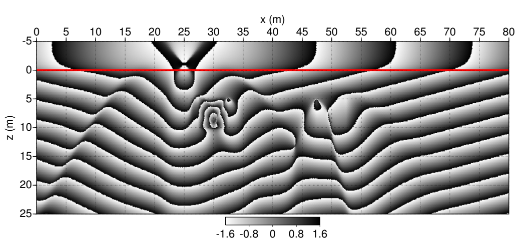

(c) Phase - component $\mathbf{h_z}$

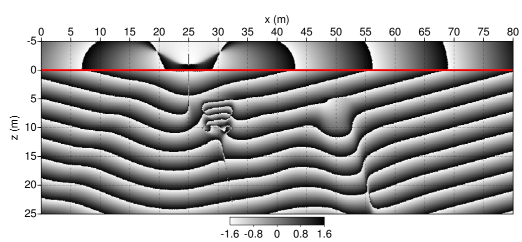

(d) Phase - component $\mathbf{h_x}$

Figure 16: Modulus and phase of the vertical and horizontal components of the magnetic field $\mathbf{h_z}$ and $\mathbf{h_x}$ computed in the exact model of figure 12 at 12 MHz.

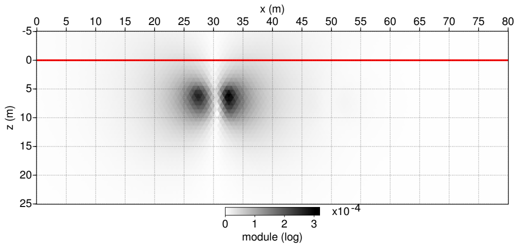

(a) Modulus - component $\mathbf{h_z}$

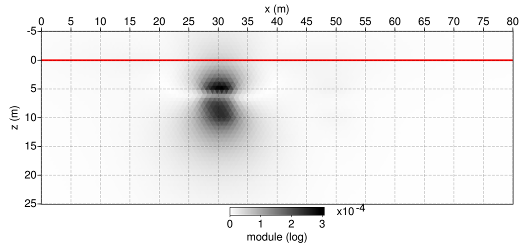

(b) Modulus - component $\mathbf{h_x}$

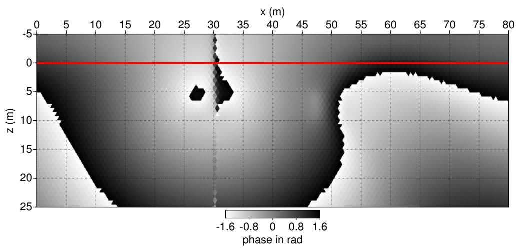

(c) Phase - component $\mathbf{h_z}$

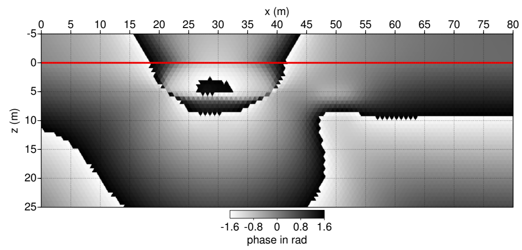

(d) Phase - component $\mathbf{h_x}$

Figure 17: Modulus and phase of the vertical and horizontal components of the magnetic field $\mathbf{h_z}$ and $\mathbf{h_x}$ computed in the exact model of figure 12 at 500 kHz.

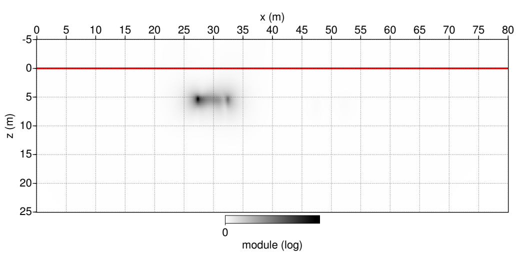

(a) Modulus - component $\mathbf{h_z}$

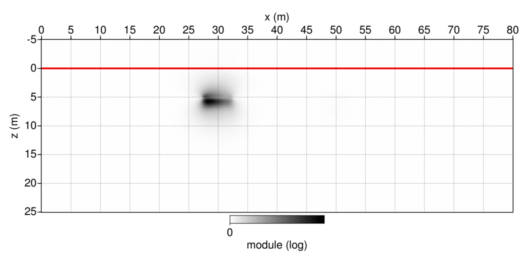

(b) Modulus - component $\mathbf{h_x}$

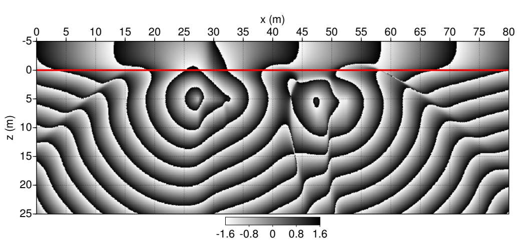

(c) Phase - component $\mathbf{h_z}$

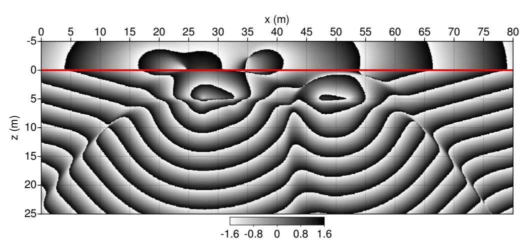

(d) Phase - component $\mathbf{h_x}$

Figure 18: Modulus and phase of the vertical and horizontal components of the magnetic field $\mathbf{h_z}$ and $\mathbf{h_x}$ computed in the exact model of figure 12 at 12 MHz.

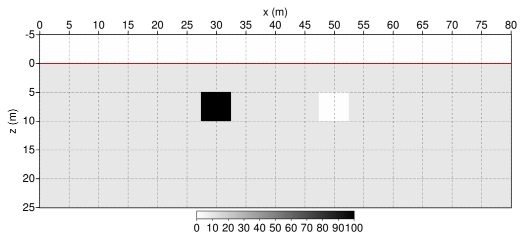

(a) Exact ε_r.

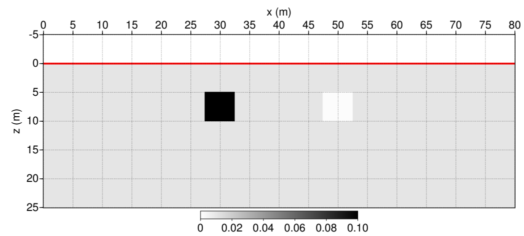

(b) Exact σ.

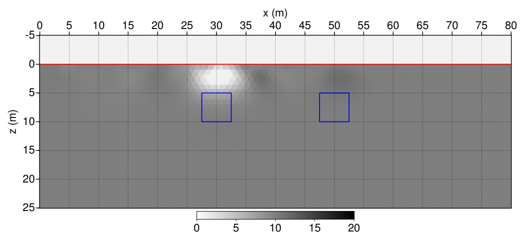

(c) Final ε_r at 500 kHz.

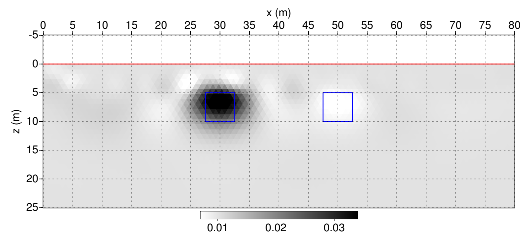

(d) Final σ at 500 kHz.

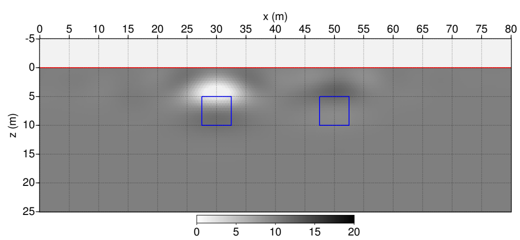

(e) Final ε_r at 2 MHz.

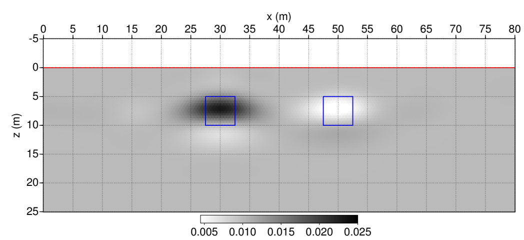

(f) Final σ at 2 MHz.

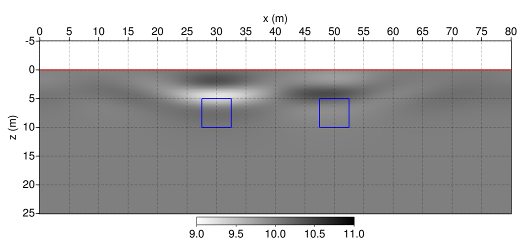

(g) Final ε_r at 6 MHz.

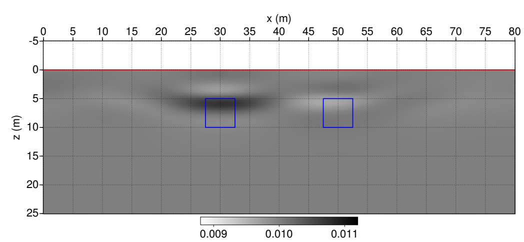

(h) Final σ at 6 MHz.

Figure 19: Final inversion results for each independant frequency.

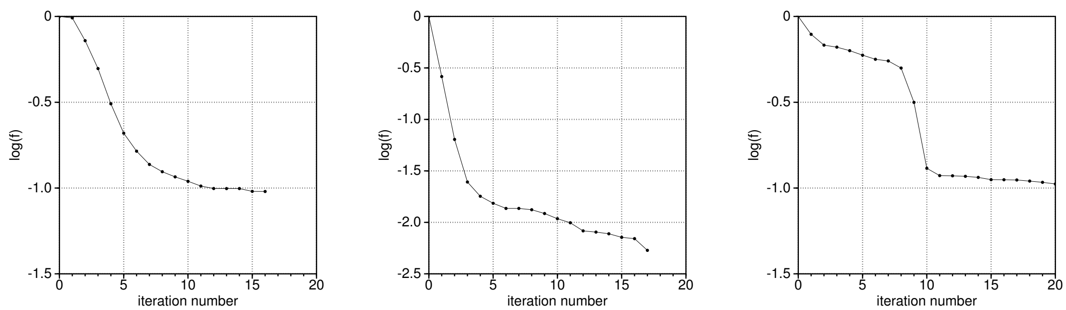

(a) Misfit at 500 kHz (b) Misfit at 2 MHz (c) Misfit at 6 MHz

Figure 20: Misfit function decrease (log) for each independant frequency.

decrease is given figure 20. As expected, the conductivity is well reconstructed at 500 kHz, but the permittivity can't be imaged at all. Only a small artefact appears on the inverted model ε_r just above the permittive anomaly. The misfit is reduced when the conductivity is explained, but its decrease is limited because of the permittivity model that can't be explained.
At 2 MHz, the upper part of the conductivity anomalies are imaged with a good accuracy and resolution, but the lower parts are not perfectly reconstructed. This is an effect of the surface acquisition combined with the limited penetration depth of the electromagnetic waves at this frequency. The inversion is also sensitive to the permittivity anomalies but the final model is dominated by artefacts just above the targets. The misfit decreases of more than 2 orders of magnitude.
At 6 MHz and 12 MHz, only the highest wavenumbers of the image (i.e. the sharp permittivity variations but not the smooth variations) can be reconstructed, because of the very small wavelengths that are propagating. Thus anomalies at the top of the targets are detected but the quantitative imaging of the square anomalies is not possible. The data misfit is poorly reduced, which is a symptom of a convergence into a local minimum.

Sequential inversion

The previous inversion test using only one frequency highlights both the sensitivity of the approach to the 2 parameters, but also the nonlinearity of the inversion that make difficult a robust inversion using a single frequency. Alternative approaches are possible to mitigate this nonlinearity, based for instance on simultanuous inversion of data at several frequencies. An other possibility to mitigate the nonlinearity is to introduced sequentially and hierarchically in the inversion subsets of the data. The data subsets are chosen to be introduced sequentially starting from the the more linear to the less linear. Possible strategies rely on a hierarchical introduction of data starting from the lowest frequency to the highest frequency (Sirgue and Pratt, 2004), by groups of frequencies (Brossier et al., 2009), by increasing or decreasing offsets (Gélis, 2005), by departure and arrival angles (Brossier and Roux, 2011), or inversion parameter by parameter (Kamei and Pratt, 2008).

We present here an inversion scheme based on sequential inversion frequency by frequency. We know that at 500 kHz, the permittivity does not have an large influence on the data ($\eta << 1$), that is the wave field is mainly diffusive and driven by the conductivity. So we first inverse only σ at 500 kHz. Then the inverted conductivity model is used as an initial model, and we jointly inverse both σ and ε_r at 500 kHz. The 2 inverted models are again used as starting model for the joint inversion of the 2 parameters, at 2 MHz, than at 6 MHz and finaly at 12 MHz.

CONCLUSIONS

ANNEXES

The acoustic - electromagnetic analogy

In the presence of electromagnetic sources, the Maxwell equations in the frequency domain read:

$$\nabla \times \mathbf{E} \; - \; i\mu\omega\mathbf{H} \;\; = \;\; -i\mu\omega\mathbf{M} \tag{22}$$
$$\nabla \times \mathbf{H} \; - \; (\sigma + i\varepsilon\omega)\mathbf{E} \;\; = \;\; \mathbf{J} \tag{23}$$

with $\mathbf{J}$ being an electric current source and $\mathbf{M}$ a magnetic moment.

If we consider 2D popagation in the observation plane (x0z), we need to assume that neither the medium properties nor the fields do vary in the y-direction ($\frac{\partial}{\partial y} = 0$). The so-called Transverse Electric mode (TE) is the 2D configuration for which the electric vector field $\mathbf{E}$ is polarized in the direction normal to the observation plane, and the magnetic field $\mathbf{H}$ is polarized in the observation plane. Thus the 6 Maxwell equations 23 can reduce to the 3 equations:

$$i\mu\omega H_x + \frac{\partial E_y}{\partial z} \;\; = \;\; i\mu\omega M_x \tag{24}$$
$$-i\mu\omega H_z + \frac{\partial E_y}{\partial x} \;\; = \;\; -i\mu\omega M_z \tag{25}$$
$$\frac{\partial H_z}{\partial x} - \frac{\partial H_x}{\partial z} - (\sigma + i\varepsilon\omega)E_y \;\; = \;\; J_y \; . \tag{26}$$

A similar equation system can be obtained for the acoustic velocity-stress system:

$$i\rho\omega V_z + \frac{\partial P}{\partial z} \;\; = \;\; -\rho F_z \tag{27}$$
$$i\rho\omega V_x + \frac{\partial P}{\partial x} \;\; = \;\; -\rho F_x \tag{28}$$
$$\frac{\partial V_z}{\partial z} + \frac{\partial V_x}{\partial x} + i\omega\frac{P}{\kappa} \;\; = \;\; i\omega\frac{P_s}{\kappa} \; , \tag{29}$$

with P the pressure field (in Pa), V_x and V_z the 2 componants of the vector particle velocity field (in m/s), ρ the mass density (in kg/m^3), and κ the complex bulk modulus (in Pa). F_z and F_x are vertical and horizontal force sources and P_s and pressure source.

This analogy in purely mathematic, the physics being different. However, we can take benefit of this analogy to use any acoustic numerical modeling tool in the frequency domain, if based on a velocity-stress formulation, to simulate electromagnetic wave propagation in 2D. The correspondance between acoustic and electromagnetic parameters and variables are summarized in table 2.

Acoustic	EM in TE mode
P	E_y
Vz	H_x
Vx	$-H_z$
ρ	μ
κ	$\frac{1}{\frac{i\sigma}{\omega}-\varepsilon}$
P_s	$\frac{-J_y}{\sigma+i\omega\varepsilon}$
F_z	$-i\omega M_x$
F_x	$+i\omega M_z$

Table 2: Correspondance between acoustic and electromagnetic variables.

Analytical solution of the inhomogeneous electromagnetic wave equation in homogeneous medium

General framework

Analytical solution of the vector field EM helmoltz equation generated from a magnetic source can be derived more easily from the Schelkunoff vector potential field $\mathbf{F}$ (Ward and Hohmann, 1988) using the relations:

$$\mathbf{E_m} = -\nabla \times \mathbf{F} \tag{30}$$

$$\mathbf{H_m} = -(\sigma + i\omega\varepsilon)\mathbf{F} + \frac{1}{i\omega\mu}\nabla\left(\nabla\cdot \mathbf{F}\right) \tag{31}$$

because the solution for the potential fields are always oriented in the same direction as the source dipole.

The Green's function satisfies the scalar differential equation:

$$\nabla^2 G \;+\; k^2 G \;=\; -\delta(x,y,z). \tag{32}$$

Its solution is in 3D:

$$G_{3D}(r) = \frac{e^{-ikr}}{4\pi r}, \tag{33}$$

with $r = \sqrt{x^2+y^2+z^2}$, and in 2D:

$$G_{2D}(r) = \frac{1}{2\pi} K_0[ikr] \tag{34}$$

with $r = \sqrt{x^2+z^2}$ and $K_0(\alpha)$ the modified Bessel function of second kind of order 0.

3D solution

A small loop of current I at the origin and in the x-y plane can be represented by an infinitesimal magnetic dipole in the direction z with a moment:

$$m = IS. \tag{35}$$

The magnetization vector is:

$$\mathbf{M_z} = m\mathbf{u_z}\delta(x, y, z). \tag{36}$$

Thus the differential equation for $\mathbf{F}$ is:

$$\nabla^2 F \; + \; k^2 F \; = \; i\omega\mu\mathbf{M_z}, \tag{37}$$

and by analogy, its solution in 3D is:

$$F_{3D}(r) = \frac{i\omega\mu m}{4\pi r} e^{-ikr}\mathbf{u_z}. \tag{38}$$

From the expression 31 and 31, the 3 components of the magnetic and electric fields are:

$$H_{x_{3D}}(r) \;=\; \frac{m}{4\pi r^3}\, e^{-ikr} \left[\frac{x\,z}{r^2}(3 + 3ikr - k^2r^2) \right] \tag{39}$$

$$H_{y_{3D}}(r) \;=\; \frac{m}{4\pi r^3}\, e^{-ikr} \left[\frac{y\,z}{r^2}(3 + 3ikr - k^2r^2) \right] \tag{40}$$

$$H_{z_{3D}}(r) \;=\; \frac{m}{4\pi r^3}\, e^{-ikr} \left[\frac{z^2}{r^2}(3 + 3ikr - k^2r^2) \;-\; (1 + ikr - k^2r^2) \right] \tag{41}$$

and

$$E_{x_{3D}}(r) \;=\; -\frac{i\omega\mu m}{4\pi r^3}\, e^{-ikr} \left[y \;+\; \frac{iky^2}{r} \right] \tag{42}$$

$$E_{y_{3D}}(r) \;=\; +\frac{i\omega\mu m}{4\pi r^3}\, e^{-ikr} \left[x \;+\; \frac{ikx^2}{r} \right] \tag{43}$$

$$E_{z_{3D}}(r) \;=\; 0 \tag{44}$$

2D solution

By analogy, the solution for $\mathbf{F}$ in 2D is:

$$F_{2D}(r) = \frac{i\omega\mu m}{2\pi} K_0[ikr]\mathbf{u_z}. \tag{45}$$

To derive the expression of the magnetic field, we use the fact that:

$$\frac{\partial K_i[\alpha]}{\partial \alpha} = -K_{i+1}[\alpha]. \tag{46}$$

This properties gives:

$$\frac{\partial K_0[ikr(x, z)]}{\partial z} = \frac{\partial K_0[\alpha]}{\partial \alpha} \cdot \frac{\partial \alpha}{\partial z} = -\frac{ikz}{r} K_1[ikr]. \tag{47}$$

Then similarly, from the expressions 31 and 31, the 2 in-plane components of the magnetic fields and the transverse component of the electric field are:

$$H_{x_{2D}}(r) = \frac{m}{2\pi}\left(\frac{ikxz}{r^3}K_1[ikr] - \frac{k^2xz}{r^2}K_2[ikr]\right) \tag{48}$$

$$H_{z_{2D}}(r) = \frac{m}{2\pi}\left(\frac{ikz^2}{r^3}K_1[ikr] - \frac{k^2z^2}{r^2}K_2[ikr] - \frac{ik}{r}K_1[ikr] + k^2K_0[ikr]\right) \tag{49}$$

$$E_{y_{2D}}(r) = \frac{\omega\mu m}{2\pi}\frac{kx}{r}K_1[ikr] \tag{50}$$

Sensitivity test for 1D layered model inversion

In this part we analyse the convexity of the misfit function in the case of surface acquisition for the problem of joint inversion of both resistivity and permittivity. The idea behind this test is to evaluate the degree of nonlinearity of the inverse problem, and evaluate the limits of the local optimzation approach. A very smooth shape of the misfit with very few local minima will argue in favor of the local linearized inversion, whereas nonconvex misfit with several local minima highlight a highly non linear behavior for which stochastic inversion might be more suitable.

For that, we define a simple 1D layered model with properties:

	ε_r	ρ ($\Omega.m$)	thickness (m)
air	1.	∞	10 m
layer 1	5.	100.	10 m
layer 2	10.	50.	

One emitter and 40 receivers are located at 1 m above the ground surface every 1 m. The source is a vertical magnetic dipole. A semi-analytical method is used to compute accurate 3D solutions for the two components of the magnetic field. We analyse the sensitivity in two configurations by varying 3 parameters and ploting the total misfit for all possible models and for several frequencies from 500 kHz to 20 MHz. In the first case we vary the thickness (1.25 m to 18.75 m) of the first layer and its relative permittivity (1 to 20) and resistivity (5 to 250 $\Omega.m$). In the second case we vary the thickness (1.25 m to 18.75 m) of the first layer and the relative permittivity (1 to 20) and the resistivity of the deepest layer (5 to 250 $\Omega.m$). Figures 21 to 28 present the misfit as a function of the three parameters and at several frequencies in the 2 tested configurations.

For the first case (inversion of the parameters of the first layer), the misfit has few local minima and the global minimum is easily identified. At low frequencies, as expected, the misfit is very sensitive to the resistivity, but very few sensitive to the permittivity variations.

It is sensitive to the thickness of the layer only when the interface reaches limited depth (a few meters), and is very poorly sensitive for larger thicknesses. At higher frequencies (>2.5 MHz), the global minimum is extremely narrow. It is still very sensitive to the resistivity, but is sensitive to the permittivity and the thickness only close to the solution and decrease slowly toward local minima otherwise. The combined use of data at several frequencies (in the example 500 kHz, 1 MHz, 2.5 MHz, 5 MHz, 10 MHz and 20 MHz) mitigates this nonlinear behavior and allows a quite large basin of attraction of the global minimum with relatively good sensitivity to both resistivity and permittivity, however, it is still poorly sensitive to the thickness.

For the second case (inversion of the parameters of the second layer and thickness of the first layer), the misfit has several local minima. As expected, the misfit is very sensitive to the resistivity, but very few sensitive to the permittivity variations at low frequency. Sensitivity to relative permittivity appears only at frequency higher thatn 5 MHz. Deep and narrow basins of attraction are visible, in particular for small thicknesses, but does not all correspond to the global minimum. Concerning the thickness, the misfit decreases nicely in the direction of the global minimum starting from underestimated thicknesses, but is no sensitive anymore when starting from thicknesses larger than the true thickness. The combined use of several frequencies does not prevent from convergence to a wrong local minimum or the non-sensitivity to thickness.

Clear information can be learned from those tests. Obviously, even the misfit is quite smooth and has a globaly convex shape, the choice of the starting model in the local iterative inversion process is crucial. For instance we see that starting from underestimated thickness let a chance to converge to the solution whereas its overestimation is inevitably doomed to failure. High sensitivity to the resistivity on the whole frequency range and on the whole range of resistivity values tested is not surprising. The low frequencies provide large and smooth misfit that let a chance to converge to the solution. Higer frequencies provide narrower minimum associated to the higher resolution expected. We can expect that the multi-frequency approach would be interesting to obtain a high resolution resistivity profile even with a local optimization technique. On the other hand, it is evident that sensitivity to permittivity and thickness decreases rapidly with depth, and that many local minima exist. Therefore, I think a stochastic approach should be more appropriate if those parameters are investigated too, at least in a first step in order to find the region of the global minimum when no accurate a priori information is available. In a second step, the local optimization should be used to get more accurate final estimations. Otherwise, more elaborated hierarchical approaches would be necessary to drive the inversion. For example, sequential inversion of resistivity and permittivity or hierarchical introduction of frequencies may mitigate the nonlinearity at each step.

ACKNOWLEDGEMENTS

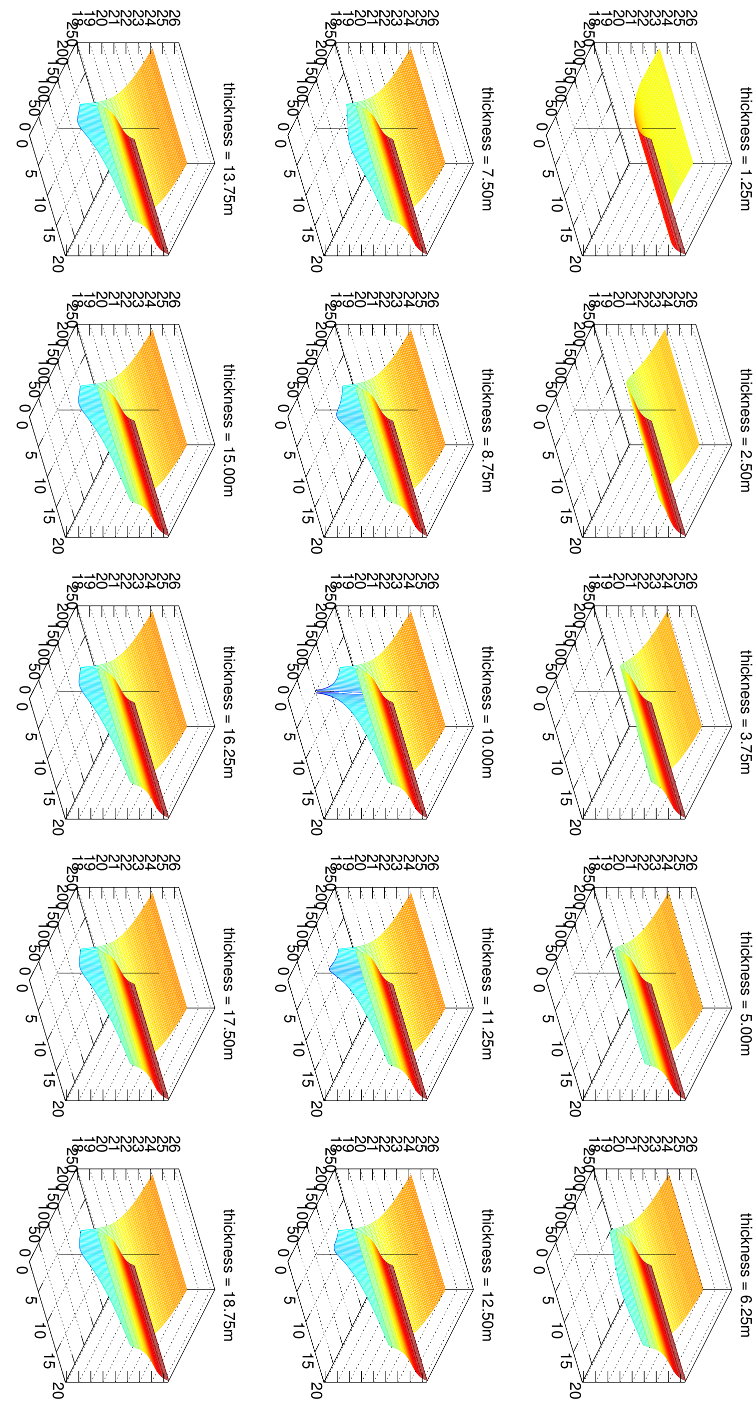

Figure 21: Misfit function as a function of the 3 parameters for the 1st case: (thickness, permittivity and resistivity of 1st layer) - 500 kHz. The solution is thickness=10 m, ε_{r_1}=5., ρ_1=100. $\Omega.m$ and is represented by the black line.

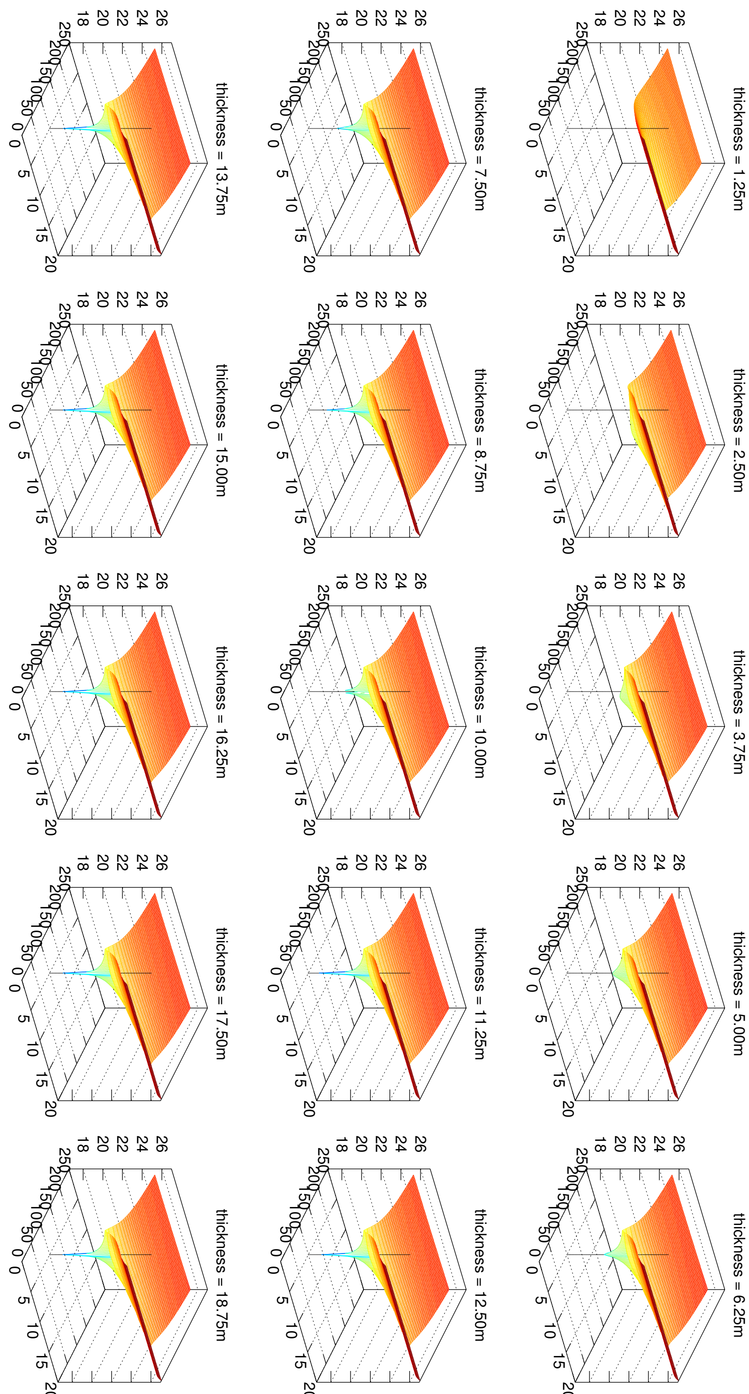

Figure 22: Misfit function as a function of the 3 parameters for the 1st case: (thickness, permittivity and resistivity of 1st layer) - 2.5 MHz. The solution is thickness=10 m, ε_{r_1}=5., ρ_1=100. $\Omega.m$ and is represented by the black line.

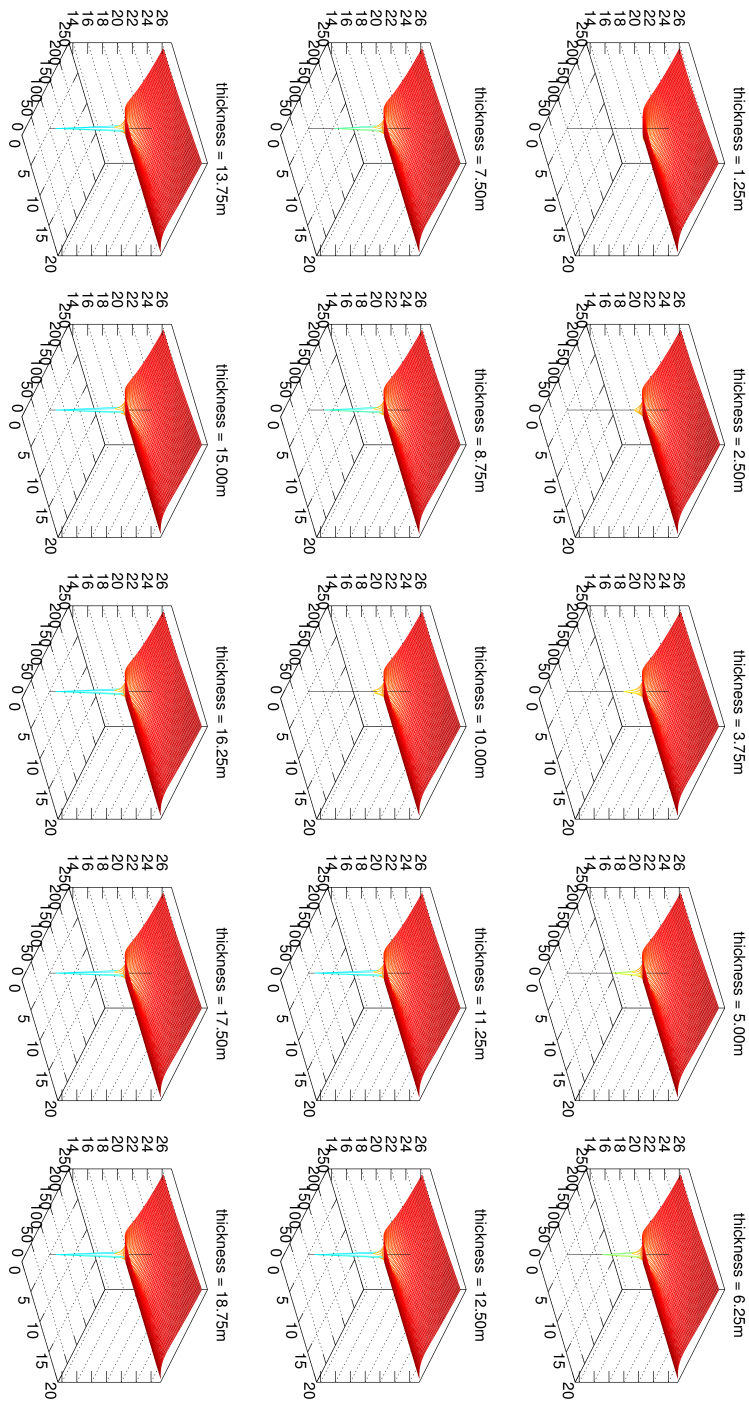

Figure 23: Misfit function as a function of the 3 parameters for the 1st case: (thickness, permittivity and resistivity of 1st layer) - 10 MHz. The solution is thickness=10 m, ε_{r_1}=5., ρ_1=100. $\Omega.m$ and is represented by the black line.

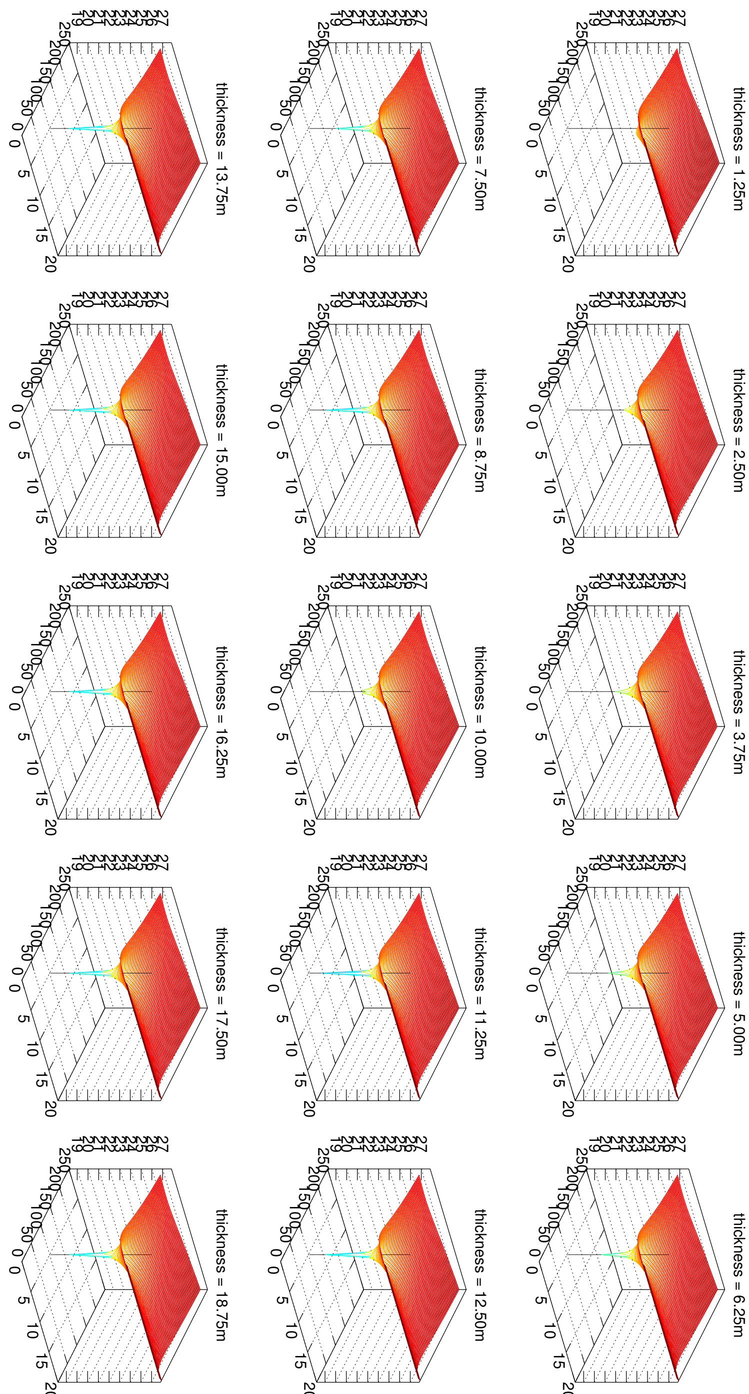

Figure 24: Misfit function as a function of the 3 parameters for the 1st case: (thickness, permittivity and resistivity of 1st layer) - full frequency range (500 kHz - 20 MHz). The solution is thickness=10 m, ε_{r_1}=5., ρ_1=100. $\Omega.m$ and is represented by the black line.

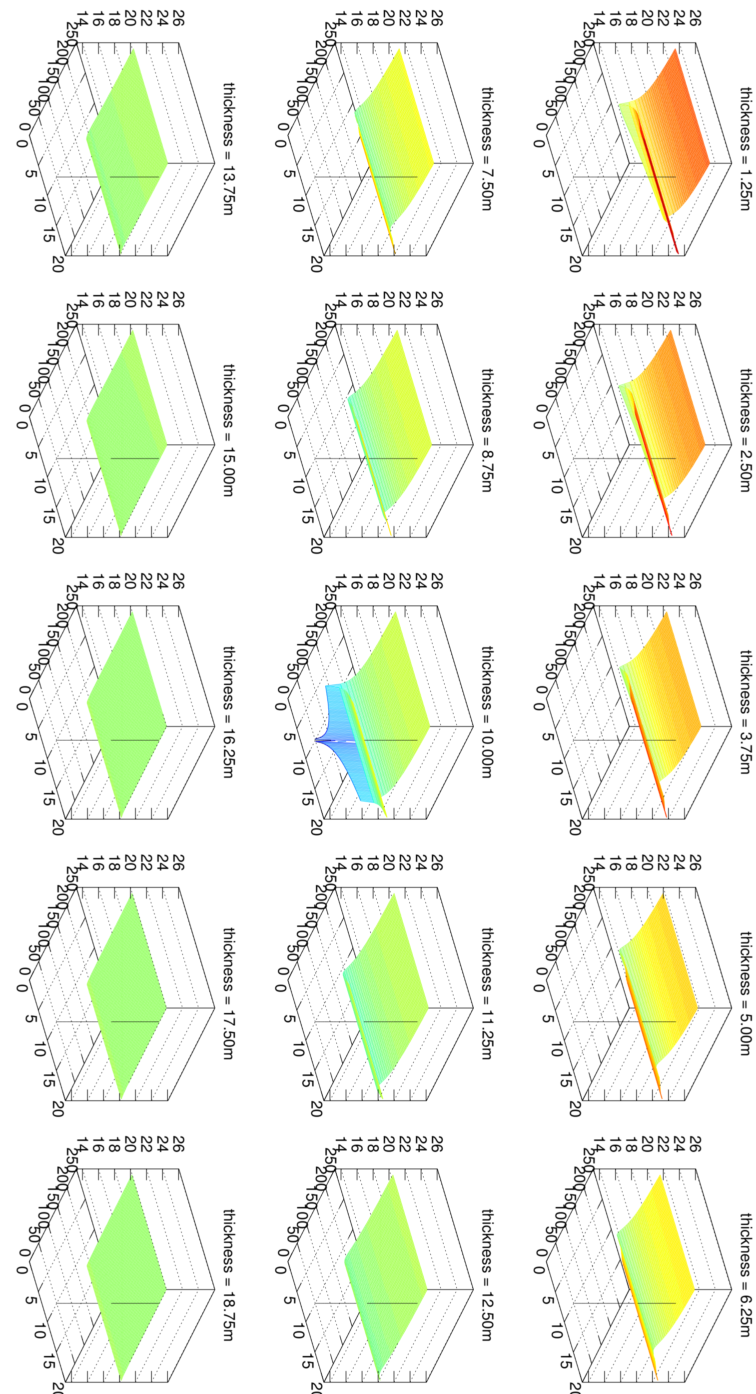

Figure 25: Misfit function as a function of the 3 parameters for the 2nd case: (thickness of the 1st layer, permittivity and resistivity of 2nd layer) - 500 kHz. The solution is thickness=10 m, ε_{r_2}=10., ρ_2=50. $\Omega.m$ and is represented by the black line.

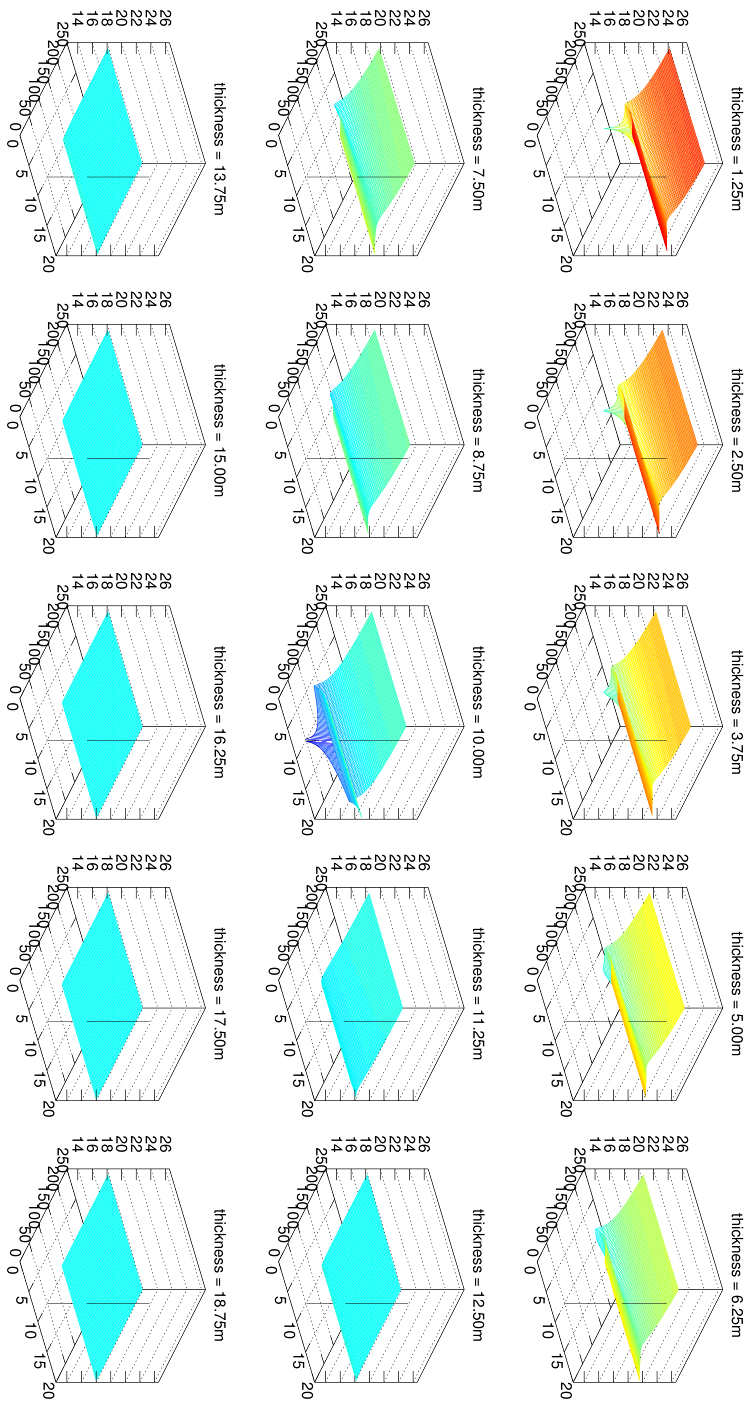

Figure 26: Misfit function as a function of the 3 parameters for the 2nd case: (thickness of the 1st layer, permittivity and resistivity of 2nd layer) - 2.5 MHz. The solution is thickness=10 m, ε_{r_2}=10., ρ_2=50. $\Omega.m$ and is represented by the black line.

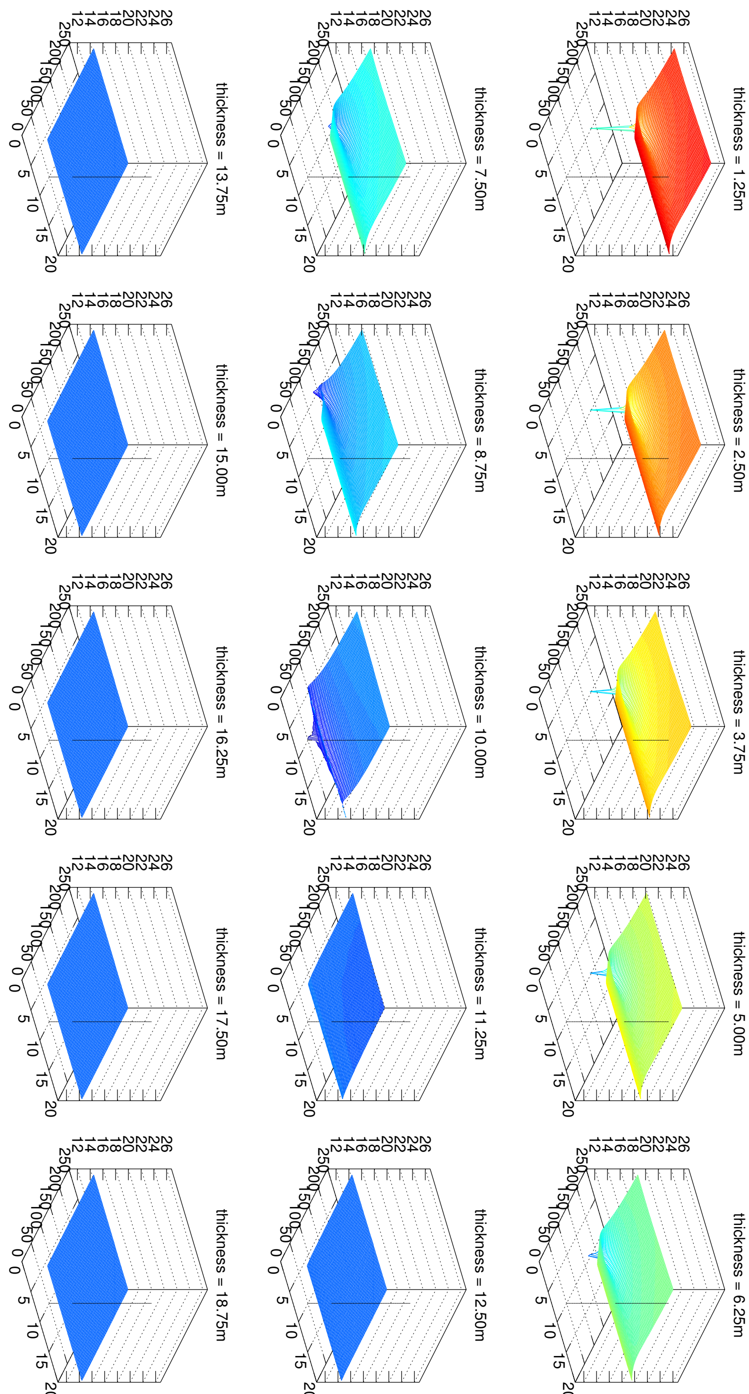

Figure 27: Misfit function as a function of the 3 parameters for the 2nd case: (thickness of the 1st layer, permittivity and resistivity of 2nd layer) - 10 MHz. The solution is thickness=10 m, ε_{r_2}=10., ρ_2=50. $\Omega.m$ and is represented by the black line.

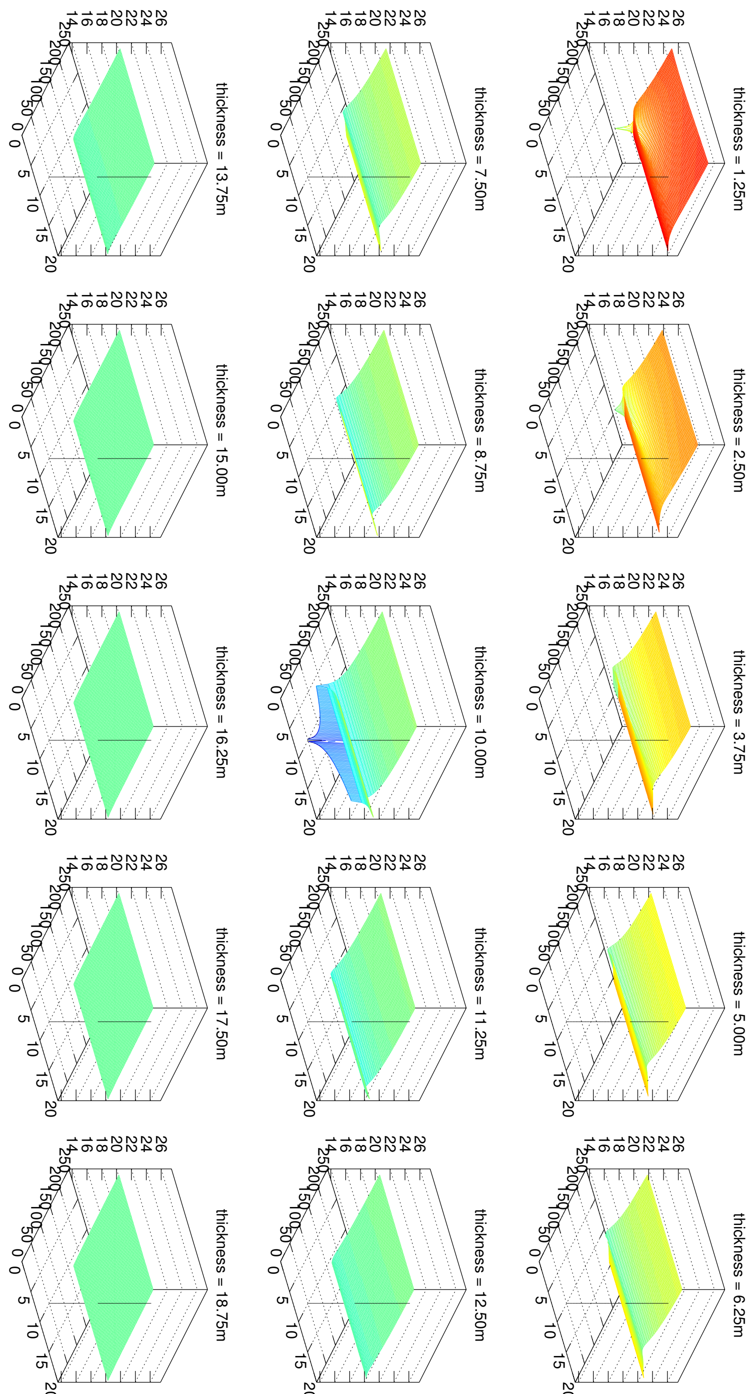

Figure 28: Misfit function as a function of the 3 parameters for the 2nd case: (thickness of the 1st layer, permittivity and resistivity of 2nd layer) - full frequency range (500 kHz - 20 MHz). The solution is thickness=10 m, ε_{r_2}=10., ρ_2=50. $\Omega.m$ and is represented by the black line.

REFERENCES

Abubakar, A., T. Habashy, L. Knizhnerman, and D. Alumbaugh, 2008, 2.5D forward and inverse modeling for interpreting low-frequency electromagnetic measurements.: Geophysics, **73**, F165–F177.

Amestoy, P., I. Duff, and J. L'Excellent, 2000, Multifrontal parallel distributed symmetric and unsymmetric solvers: Computer Methods in Applied Mechanics and Engineering, **184**, 1223–1238.

Avdeev, D., 2005, Three-dimensional electromagnetic modeling and inversion from theory to application.: Survey in Geophysics, **26**, 767–799.

Avdeev, D. and A. Avdeeva, 2009, 3d magnetotelluric inversion using a limited-memory quasi-newton optimization.: Geophysics, **74**, F45–F57.

Avdeev, D., A. Kuvshinov, O. Pankratov, and G. Newman, 2002, Three-dimensional induction logging problems, part I - an integral equation solution and model comparisons.: Geophysics, **67**, 413–426.

Badea, E., M. Everett, G. Newman, and O. Biro, 2001, Finite-element analysis of controlled source electromagnetic induction using coulomb-gauged potentials.: Geophysics, **66**, 786–799.

Berenger, J., 1994, A perfectly matched layer for absorption of electromagnetic waves: Journal of Computational Physics, **114**, 185–200.

Bitri, A. and G. Grandjean, 1998, Frequency-wavenumber modeling and migration of 2d gpr data in moderately heterogeneous dispersive media.: Geophysical Prospecting, **46**, 287–301.

Borner, R.-U., O. Ernst, and K. Spitzer, 2008, Fast 3d simulation of transiant electromagnetic fields by model reduction in the frequency domain using krylov subspace projection: Geophysical Journal International, **173**, 740–752.

Bourgeois, B., 2002, Etude de faisabilité d'un appareil électromagnetique fréquentiel dans la gamme 30 khz - 10 mhz.: Technical Report BRGM/RC-51643-FR, BRGM.

Brossier, R., 2011, Two-dimensional frequency-domain visco-elastic full waveform inversion: Parallel algorithms, optimization and performance: Computer & Geosciences, **37**, 444–455.

Brossier, R., S. Operto, and J. Virieux, 2009, Seismic imaging of complex onshore structures by two-dimensional elastic frequency-domain full-waveform inversion: Geophysics, **74**, WCC105–WCC118.

Brossier, R. and P. Roux, 2011, Shallow-water tomography using double beamforming and full waveform inversion: Journal of Computational Acoustics, **submitted**.

Brossier, R., J. Virieux, and S. Opertro, 2008, Parsimonious finite-volume frequency-domain method for (2-D) (P-SV)-wave modelling: Geophysical Journal International, **175**, 541–559.

Cai, W. and G. McMechan, 1995, Ray-based synthesis of bistatic ground-penetrating radar profiles.: Geophysics, **60**, 87–96.

Chave, A. and C. Cox, 1982, Controlled electromagnetic sources for measureing electrical conductivity beneath the oceans,1. forward problem and model study.: Journal of Geophysical Research, **87**, 5327–5338.

Constable, S. and L. Srnka, 2007, An introduction to marine controlled source electromagnetic methods for hydrocarbon exploration.: Geophysics, **72**, WA3–WA12.

Cordua, K., T. Hansen, and K. Mosegaard, 2012, Monte carlo full-waveform inversion of crosshole gpr data using multiple-point geostatistical a priori information.: Geophysics,

77, H19–H31.

Dahlin, T., 2001, The development of dc resistivity imaging techniques.: Computer & Geosciences, **27**, 1019–1029.

Ernst, J., A. Green, H. Maurer, and K. Holliger, 2007, Application of a new 2d time-domain full-waveform inversion scheme to crosshole radar data: Geophysics, **72**, J53–J64.

Fisher, E., G. McMechan, and A. Annan, 1992a, Acquisition and processing of wide-aperture ground-penetrating radar data.: Geophysics, **57**, 495–504.

Fisher, E., G. McMechan, A. Annan, and S. Cosway, 1992b, Examples of reverse-time migration of single-channel ground-penetrating radar profiles.: Geophysics, **57**, 577–586.

Gélis, C., 2005, Inversion des formes d'onde elastique dans le domaine espace-frequence en deux dimensions. application à la caracterisation de la subsurface dans le cadre de la detection des cavités souterraines.: PhD thesis, University of Nice Sophia-Antipolis.

Grayver, A., R. Streich, and O. Ritter, 2013, Three-dimensional parallel distributed inversion of csem data using a direct forward solver.: Geophysical Journal International, **193**, 1432–1446.

Holliger, K., M. Musil, and H. Maurer, 2001, Ray-based amplitude tomography for crosshole georadar data: a numerical assessment.: Journal of Applied Geophysics, **47**, 285–298.

Huang, H. and D. Fraser, 2001, Mapping of the resistivity, susceptibility, and permittivity of the earth using a helicopter-borne electromagnetic system.: Geophysics, **66**, 148–157.

———, 2002, Dielectric permittivity and resistivity mapping using high-frequency, helicopter-borne em data.: Geophysics, **67**, 727–738.

Kamei, R. and R. Pratt, 2008, Waveform tomography strategies for imaging attenuation structure with cross-hole data: Presented at the Proceeding of the 70th EAGE Conference and Exhibition in Rome.

Kessouri, P., S. Buvat, and A. Tabbagh, 2012, Simultaneous mapping of the soil electrical conductivity and dielectric permittivity using a medium frequency em device.: Presented at the Near Surface Geoscience 2012 – 18th European Meeting of Environmental and Engineering Geophysics, Paris (France).

Lampe, B., K. Holliger, and A. Green, 2003, A finite-difference timpe-domain simulation tool for ground-penetrating radar antennas.: Geophysics, **68**, 971–987.

Lavoué, F., R. Brossier, L. Métivier, S. Garambois, and J. Virieux, 2014, Two-dimensional permittivity and conductivity imaging by full waveform inversion of multioffset GPR data: a frequency-domain quasi-newton approach.: Geophysical Journal International, **197**, 248–268.

Loke, M. and R. Barker, 1996, Practical techniques for 3d resistivity surveys and data inversion: Geophysical Prospecting, **44**, 499–523.

Lopes, F., 2009, Inversion des formes d'ondes électromagnetique de donnés radar (GPR) multioffsets.: PhD thesis, Université Denis Diderot Paris 7.

Loseth, L. and B. Ursin, 2007, Electromagnetic fields in planarly layered anisotropic media.: Geophysical Journal International, **170**, 44–80.

Meles, G., S. Greenhalgh, A. Green, H. Maurer, and J. V. D. Kruk, 2011, Taming the nonlinearity problem in gpr full waveform inversion for high contrast media.: Journal of Applied Geophysics, **73**, 174–186.

Meles, G., J. V. D. Kruk, S. Greenhalgh, J. Ernst, H. Maurer, and A. Green, 2010, A new vector full waveform inversion algorithm for simultaneous updating of conductivity and permittivity parameters for combination crosshole/borehole-to-surface gpr data.: IEEE Transactions on Geoscience and Remote Sensing., **48**, 3391–3407.

Metivier, L., F. Bretaudeau, R. Brossier, S. Operto, and J. Virieux, 2014, Full waveform inversion and the truncated newton: quantitative imaging of complex subsurface structures: Geophysical Prospecting. in press.

Mitsuhata, Y. and T. Ushida, 2004, 3d magnetotelluric modeling using the t-ω finite-element method.: Geophysics, **69**.

Newman, G. and D. Alumbaugh, 1995, Frequency-domain modeling or airborne electromagnetic responses using staggered finite differences.: Geophysical Prospecting, **43**, 1021–1041.

Nocedal, J. and S. Wright, 1999, Numerical optimization: Springer.

Oldenburg, D., E. Haber, and R. Shekhtman, 2007, Rapid forward modeling of multisource tem data: Proceedings of the 4th International Symposium on Three-dimensional electromagnetic, 35–38.

Paige, C. C. and M. A. Saunders, 1982a, ALGORITHM 583 LSQR : Sparse linear equations and least squares problems: ACM Transactions on Mathematical Software, **8**, 195–209.

———, 1982b, LSQR: an algorithm for sparse linear equations and sparse least squares: ACM Transactions on Mathematical software, **8**, 43–71.

Plessix, R. and W. Mulder, 2008, Resistivity imaging with controlled-source electromagnetic data: depth and data weigthing.: Inverse Problems, **24**, 034012.

Plessix, R.-E., 2006, A review of the adjoint-state method for computing the gradient of a functional with geophysical applications: Geophysical Journal International, **167**, 495–503.

Pratt, R., C. Shin, and G. Hicks, 1998, Gauss-Newton and full Newton methods in frequency-space seismic waveform inversion: Geophysical Journal International, **133**, 341–362.

Pratt, R. and M. Worthington, 1990, Inverse theory applied to multi-source cross-hole tomography. I: Acoustic wave-equation method: Geophysical Prospecting, **38**, 298–310.

Sirgue, L. and R. Pratt, 2004, Efficient waveform inversion and imaging: A strategy for selecting temporal frequencies: Geophysics, **69**, 231–248.

Song, Z. and P. Williamson, 1995, Frequency-domain acoustic-wave modeling and inversion of crosshole data: Part 1 – 2.5d modeling method: Geophysics, **60**, 784–795.

Stewart, D., W. Anderson, T. Grover, and V. Labson, 1994, Shallow subsurface mapping by electromagnetic sounding in the 300khz to 30 mhz range: Model studies and prototype system assessment.: Geophysics, **59**, 2101–1210.

Streich, R., 2009, 3d finite-difference frequency-domain modeling of controlled-source electromagnetic data: Direct solution and optimizationfor high accuracy.: Geophysics, **74**, F95–F105.

Streich, R., M. Becken, and O. Ritter, 2011, 2.5d controlled-source em modeling with general 3d source geometries.: Geophysics, **76**, F387–F393.

Tabbagh, A., 1994, Simultaneous measurement of electrical conductivity and dielectric permittivity of soils using a slingram electromagnetic device in medium frequency range: **36**, 159–170.

Tarantola, A., 1984, Inversion of seismic reflection data in the acoustic approximation: Geophysics, **49**, 1259–1266.

Virieux, J. and S. Operto, 2009, An overview of full-waveform inversion in exploration geophysics: Geophysics.

Wallin, E., 2010, Sensitivity of the high-frequency sounding method to variations in electrical properties.: Geophysics, **75**, WA189–WA197.

Wang, T. and G. Hohmann, 1993, A finite-difference time-domain solution for three-dimensional electromagnetic modeling.: Geophysics, **58**, 797–809.

Wannamaker, P., G. Hohmann, and S. Ward, 1984, Magnetotelluric responses of three-dimensional bodies in layered earths.: Geophysics, **49**, 1517–1533.

Ward, S. and G. Hohmann, 1988, Electromagnetic methods in applied geophysics, volume **1**, chapter Electromagnetic theory for geophysical applications, 131–311. SEG.

Weiss, C. and G. Newman, 2002, Electromagnetic induction in a fully 3d anisotropic earth.: Geophysics, **67**, 1104–1114.

FIGURES